POLITECNICO DI MILANO

Faculty of Industrial Engineering

Master of Science in Mechanical Engineering

CFD FEASIBILITY FOR DUST ANALYZER

Advisor:
Prof. Stefano MALAVASI
Prof. Bortolino SAGGIN

Co-Advisor:
Dr. Diego SCACCABAROZZI
Dr. Gianandrea Vittorio MESSA

Master thesis of:
Ivan LOPEZ Matr. 803669

Academic Year 2014 - 2015

A mi querida familia

Gracias a Iván por siempre hacer lo incorrecto

Gracias a Cámilo por siempre hacer lo correcto

Abstract

The thesis work aims at design the inlet duct of the MicroMed instrument using an inertial filter that provides a cut off diameter between $20 - 30\mu m$. For the development of this work we use a CFD Euler-Lagrangian approach to solve the RANS model and DPM to track the particles for the development of the inertial filter. Proposed geometry was then designed, using FE models, to resist against expected loading and assure a proper dynamic behavior.

***key words*:**

CFD, inertial filter, Mars, MicroMed, Two phase flow

Sommario

Il lavoro di tesi ha l'obiettivo di progettare il condotto di aspirazione dello strumento MicroMed utilizzando un filtro inerziale che permette di filtrare particelle di polvere di diametro compreso tra $20 - 30\mu m$. Per lo sviluppo di questo lavoro è stato utilizzato un approccio Eulerolagrangiano CFD per risolvere il modello RANS e DPM e per tracciare le particelle per lo sviluppo del filtro inerziale. La geometria proposta è stata progettata, utilizzando modelli ad elementi finiti, per resistere contro il carico previsto dalla missione e per garantire un'adeguata rigidezza della struttura.

parole chiave: CFD, filtro inerziale, Marte, MicroMed, flusso di due fase

Contents

List of Figures

List of Tables

Nomenclature

α_f	Volume fraction of the fluid	-
α_p	Volume fraction of the particles	-
$\bar{\rho}_c$	mean density of the continuous phase	kg/m^3
$\bar{P}$	Gravitational acceleration	m/s^2
ϵ	Dissipation rate	-
μ	Gas viscosity	kg/ms
μ_c	Cinematic viscosity of the continuous phase	$kg/(ms)$
μ_{tot}	Total Viscosity	$kg/(ms)$
μ_T	Turbulent viscosity	$kg/(ms)$
ρ_f	Fluid density	kg/m^3
ρ_p	Particle density	kg/m^3
$\sqrt{Stk_{50}}$	Value of $\sqrt{Stk}$ corresponding to d_{50}	m
τ_λ	Optical depth	$m^(-1)$
l	optical wavelength	-
sv_l	extinction coefficient at desired optical wavelength	$m^(-1)$
$\tilde{U_c}$	average velocity of the continuous phase	m/s
$A(z)$	cross-sectional area per unit volume	m
$a(z)$	Mean radius in gamma distribution	-
$b(z)$	Spread factor in gamma distribution	-
$b_{r,l}$	effective scattering cross-section of a single aerosol of radius r	m
C	Normalaise factor of gamma distribution	m
C_c	Cunninghanm slip correction	-

C_D	Drag force	N
d_{50}	Cut size	m
d_b	Body diameter	m
d_p	Particle diameter	m
$F(X)$	cumulative undersize distribution	-
F_g	Gravitational force	N
$f_N(x)$	Number density distribution	-
$f_V(x)$	Volume density distribution	m^3
g	Gravitational acceleration	m/s^2
k	Turbulent kinetic energy	-
$N(r,z)$	Particle sive distribution by number in the Mars atmosphere	m
N_i	Number of particles of size i	-
Q	volumetric flow rate though nozzle	m^3/s
Q_{ext}	extinction inefficiencies	-
$Q_{r,l}$	single particle scattering efficiency	-
r	Radius of particles in gamma distribution	m
Re_j	Jet Reynolds number	-
Stk	Stokes number	-
U	Relative velocity of body to gas	m/s
V	Total volumen of particles	m^3
V_{pi}	Volume of particle i	m^3
W	Nozzle diameter (circular impactor) or nozzle width (rectangular impactor)	m

z	Height of in gamma distribution	m
η	Mass loading	-

1 Introduction

The ExoMars Mission 2016-2018

The European Space Agency (ESA) has established the ExoMars program to investigate the Martian environment and to demonstrate new technologies paving the way for a future. This program aims to establish if life ever existed on Mars, which is one of the outstanding scientific questions of our time. To address this important goal, Two missions are foreseen within the ExoMars program: One consisting of an Orbiter plus an Entry, Descent and Landing Demonstrator Module, to be launched in 2016, and second one featuring a rover, with a launch date of 2018. Both missions will be carried out in cooperation with Roscosmos (The Russian Federal Space Agency). The ExoMars program will demonstrate a number of essential flight and in-situ enabling technologies that are necessary for future exploration missions, such as an international Mars Sample Return mission. This include:

Entry, descent and landing (EDL) of a payload on the surface of Mars;

- Surface mobility with a rover;
- Access to the subsurface to acquire samples;
- and Sample acquisition, preparation, distribution and analysis.

At the same time a number of important scientific investigations will be carried out, for example:

- Search for signs of past and present life on Mars;
- Investigate how the water and geochemical environment varies;
- and Investigate Martian atmospheric trace gases and their sources.

The 2016 mission includes a Trace Gas Orbiter (TGO) and an Entry, Descent and Landing Demonstrator Module (EDM). The Orbiter will carry scientific instruments to detect and study atmospheric trace gases, such as methane. The EDM will contain sensors to evaluate the lander's performance as it descends, and additional sensors to study the environment at the landing site.The 2018 mission includes a rover that will carry a drill and a suite of instruments dedicated to exobiology and geochemistry research. Roscosmos will provide a Proton launcher for both missions.[16]

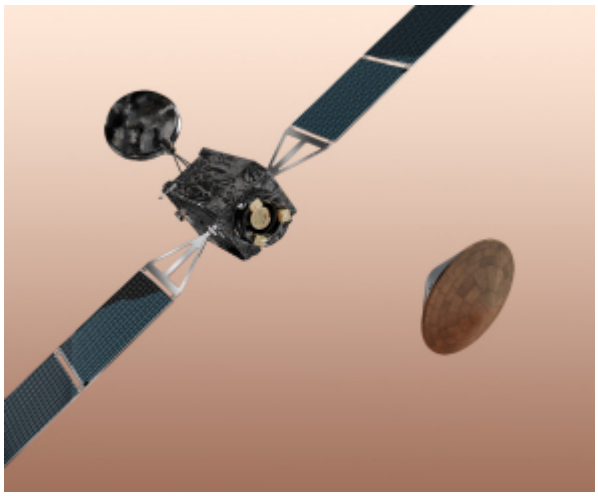

Figure 1: Trace Gas Orbiter
Picture taken from[15]

1.1 ExoMars Orbiter and EDM Mission (2016)

The first mission of the ExoMars program, scheduled to arrive at Mars in 2016, consists of a Trace Gas Orbiter (Figure 1) plus an Entry, Descent and Landing Demonstrator Module (EDM). The main objectives of this mission are to search for evidence of methane and other trace atmospheric gases that could be signatures of active biological or geological processes and to test key technologies in preparation for ESA's contribution to subsequent missions to Mars.

The Orbiter and EDM will be launched together in January 2016 on a Proton rocket and will fly to Mars in a mated configuration. By taking advantage of the positioning of Earth and Mars the cruise phase can be limited to about 9 months. Three days before reaching the atmosphere of Mars, the EDM will be ejected from the Orbiter towards the Red Planet. The EDM capsule will then coast towards its destination, entering the Martian atmosphere and landing on the surface of the planet. From its coasting to Mars till its landing, the EDM will communicate with the Orbiter. Once on the surface, the communications of the EDM will be supported from a NASA Relay Orbiter. The ExoMars Orbiter will be inserted into an elliptical orbit around Mars and then sweep through the atmosphere to finally settle into a circular, ~ 400-km altitude orbit ready to conduct its scientific mission.

The Orbiter spacecraft is designed by ESA, while Roscosmos provides the launch vehicle. A scientific payload with instruments from Russia and Europe will be accommodated on the Orbiter to achieve its scientific objectives. The ExoMars Orbiter will perform detailed, remote observations of the Martian atmosphere, searching for evidence of gases of possible biological importance, such as methane and its degradation products. The instruments on board the Orbiter will carry out a variety of measurements to investigate the location and nature of the sources that produce these gases. The scientific mission is expected to begin in mid 2017 for a period of at least one Martian year (687 Earth days). The Trace Gas Orbiter will also serve as a data relay asset for the 2018 rover mission of the ExoMars program and until the end of 2022.[15]

1.1.1 Schiaparelli: the ExoMars Entry, Descent and Landing Demonstrator Module

One of the core scientific goals of any mission to Mars is the search for evidence of life. The best approach is to investigate the surface where the evidence may lie.The key element for accessing the surface of Mars and one of the greatest challenges in space exploration is the successful execution of the entry, descent and landing sequence on the surface of the planet.This is one of the reasons why since the late 1960s there have been so many missions attempting to land on the surface of Mars, some being successful, many others ill-fated.

Schiaparelli - also known as the Entry, Descent and Landing Demonstrator Module (EDM) - is a technology demonstration vehicle carried by the ExoMars Trace Gas Orbiter, which will be launched in 2016 to demonstrate the capability of European industry to perform a controlled landing on the surface of Mars. The preparation for this mission enhances Europe's expertise and enables the testing of key technologies which could be used in subsequent missions to Mars.

Although designed to demonstrate entry, descent and landing technologies, Schiaparelli also offers limited, but useful, science capabilities. It will deliver a science package that will operate on the surface of Mars for a short duration after landing, planned to last approximately 2-8 days.

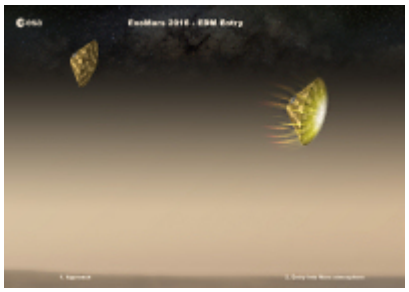

Figure 2: EDM “entry phase
Picture taken from[20]

Arriving at Mars

Schiaparelli will start its journey to Mars in January 2016 attached to the Trace Gas Orbiter. They will be launched on a Proton rocket and will arrive approximately 9 months later at Mars.

Coast

- Three days before reaching the atmosphere of Mars, Schiaparelli will separate from the Orbiter.
- On the module will then coast to Mars during this phase it will remain in hibernation mode in order to reduce its power consumption.
- Schiaparelli will be activated a few hours before entering the atmosphere of Mars at a velocity of approximately 5.8 km/s.

Entry

The ExoMars Entry, Descent and Landing Demonstrator Module, called Schiaparelli (Figure 2).

- Schiaparelli enters the atmosphere of Mars at an altitude of 120 km.
- The heat shield will protect Schiaparelli from the severe heat flux and deceleration from Mach 35 to Mach 5 (Mach 5 is motion 5 times greater than the speed of sound. Rockets and the space shuttle reach this speed as they go into orbit).

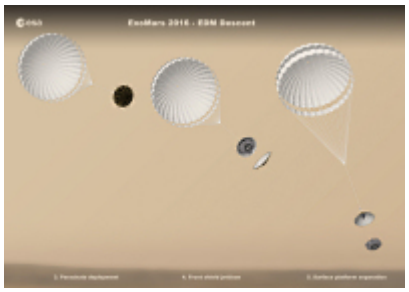

Figure 3: EDM "descent phase"
Picture taken from[20]

Descent

Schiaparelli in the descent phase (Figure 3).

- As soon as Schiaparelli has slowed down to Mach 2 (for example, the speed of a military fighter aircraft), the parachute will be deployed to further decelerate to subsonic speed (velocity less than Mach 1. This is the speed of most commercial airplanes).

- The module will first release the front heat shield and then the rear heat shield will also be jettisoned.

- Schiaparelli will activate its Doppler radar altimeter and velocimeter to locate its position with respect to the Martian surface.

Landing

Schiaparelli in the landing phase (Figure 4).

- At the optimum distance from the ground, the liquid propulsion system will be activated to reduce the speed to close to zero and to allow a controlled landing on the surface of Mars.

- The primary landing site has been identified: it is a plain known as Meridiani Planum. This area interests scientists because it contains an ancient layer of hematite, an iron oxide that, on Earth, almost always forms in an environment containing liquid water.

Figure 4: EDM "landing phase"
Picture taken from[20]

A communication link between Schiaparelli and the Trace Gas Orbiter will facilitate the real-time transmission of the most important data measured by the module. The complete set of data acquired will be transmitted to the Orbiter within 8 sols after the landing (a solar day on Mars, or sol, is 24 hours and 39 minutes). The Schiaparelli mission then comes to an end and the Orbiter sweeps through the atmosphere to reach its final science orbit.[20]

1.1.2 EDM Science Package and Science Investigations

EDM investigations were selected in June 2011 following an announcement of opportunity released by ESA and NASA. The selected investigations consist of: an EDM surface payload, to operate on the surface of Mars for 2–8 sols, and a program for entry and descent science investigations using the spacecraft engineering sensors.

EDM surface payload The EDM surface payload (Figure 5), based on the proposed DREAMS (Dust Characterization, Risk Assessment, and Environment Analyzer on the Martian Surface) package, consists of a suite of sensors to measure the wind speed and direction (MetWind), humidity (DREAMS-H), pressure (DREAMS-P), surface temperature (MarsTem), the transparency of the atmosphere (Solar Irradiance Sensor, SIS), and atmospheric electrification (Atmospheric Radiation and Electricity Sensor; MicroARES). The science package accommodated on the ExoMars Entry, Descent and Landing Demonstrator Module surface platform Credit: TAS-I, DREAMS team, ESA

DREAMS will provide the first measurements of electric fields on the

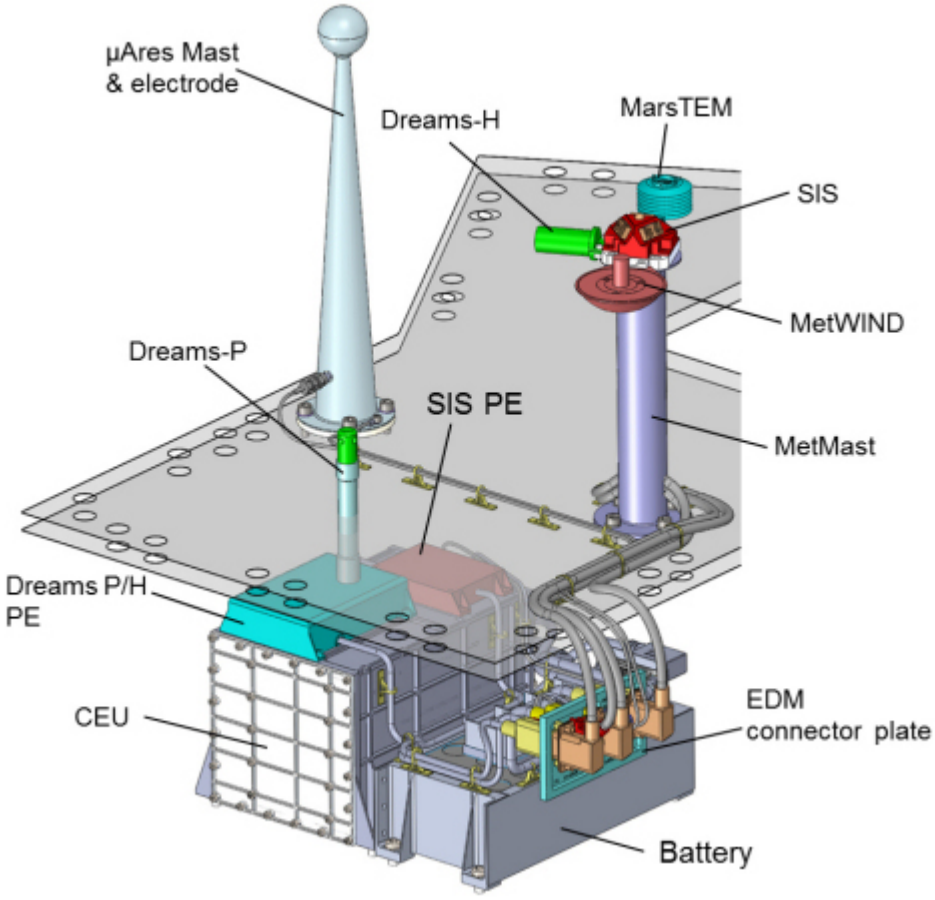

Figure 5: Science package accommodated on the ExoMars EDM
Picture taken from[13]

surface of Mars (with MicroARES). Combined with measurements (from SIS) of the concentration of atmospheric dust, DREAMS will provide new insights into the role of electric forces on dust lifting, the mechanism that initiates dust storms. In addition, the DREAMS-H sensor will complement MicroARES measurements with critical data about humidity; this will enable to understand better the dust electrification process.[13]

1.2 ExoMars Mission (2018)

The 2018 mission of the ExoMars program will deliver a European rover (Figure 6) and a Russian surface platform to the surface of Mars. A Proton rocket will be used to launch the mission, which will arrive to Mars after a nine-month journey. The ExoMars rover will travel across the Martian surface to search for signs of life. It will collect samples with a drill and analyze them with next-generation instruments. ExoMars will be the first mission to combine the capability to move across the surface and to study Mars at depth.

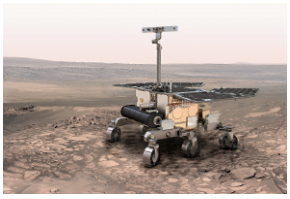

Figure 6: ESA's ExoMars Rover
Picture taken from[14]

During launch and cruise phase, a carrier module (provided by ESA with some contributions from Roscosmos) will transport the surface platform and the rover within a single aeroshell. A descent module (provided by Roscosmos with some contributions by ESA) will separate from the carrier shortly before reaching the Martian atmosphere. During the descent phase, a heat shield will protect the payload from the severe heat flux. Parachutes, thrusters, and damping systems will reduce the speed, allowing a controlled landing on the surface of Mars.

After landing, the rover will egress from the platform to start its science mission. The primary objective is to land the rover at a site with high potential for finding well-preserved organic material, particularly from the very early history of the planet. The rover will establish the physical and chemical properties of Martian samples, mainly from the subsurface. Underground samples are more likely to include biomarkers, since the tenuous Martian atmosphere offers little protection from radiation and photochemistry at the surface.

The drill is designed to extract samples from various depths, down to a maximum of two meters. It includes an infrared spectrometer to characterize the mineralogy in the borehole. Once collected, a sample is delivered to the

rover's analytical laboratory, which will perform mineralogical and chemistry determination investigations. Of special interest is the identification of organic substances. The rover is expected to travel several kilometers during its mission.

The ExoMars Trace Gas Orbiter, part of the 2016 ExoMars mission, will support communications. The Rover Operations Control Center (ROCC) will be located in Turin, Italy. The ROCC will monitor and control the ExoMars rover operations. Commands to the Rover will be transmitted through the Orbiter and the ESA space communications network operated at ESA's European Space Operations Center (ESOC).[14]

1.2.1 ExoMars Rover

The ExoMars Rover, developed by ESA, provides key mission capabilities: surface mobility, subsurface drilling and automatic sample collection, processing, and distribution to instruments. It hosts a suite of analytical instruments dedicated to exobiology and geochemistry research: this is the Pasteur payload. The ExoMars Rover Prototype (Figure 7) uses solar panels to generate the required electrical power, and is designed to survive the cold Martian nights with the help of novel batteries and heater units.

Due to the infrequent communication opportunities, only 1 or 2 short sessions per sol (Martian day), the ExoMars Rover is highly autonomous. Scientists on Earth will designate target destinations on the basis of compressed stereo images acquired by the cameras mounted on the Rover mast.

The Rover must then calculate navigation solutions and safely travel approximately 100 m per sol. To achieve this, it creates digital maps from navigation stereo cameras and computes a suitable trajectory. Close-up collision avoidance cameras are used to ensure safety.

The locomotion is achieved through six wheels. Each wheel pair is suspended on an independently pivoted bogie (the articulated assembly holding the wheel drives), and each wheel can be independently steered and driven. All wheels can be individually pivoted to adjust the Rover height and angle with respect to the local surface, and to create a sort of walking ability, particularly useful in soft, non-cohesive soils like dunes. In addition, inclinometers and gyroscopes are used to enhance the motion control robustness. Finally, Sun sensors are utilized to determine the Rover's absolute altitude on the Martian surface and the direction to Earth.

The camera system's images combined with ground penetrating radar

Figure 7: ExoMars Rover Prototype
Picture taken from[17]

data collected while traveling, will allow scientists on-ground to define suitable drilling locations.

The Rover subsurface sampling device will then autonomously drill to the required depth (maximum 2 m) while investigating the borehole wall mineralogy, and collect a small sample. This sample will be delivered to the analytical laboratory in the heart of the vehicle. The laboratory hosts four different instruments and several support mechanisms. The sample will be crushed into a fine powder. By means of a dosing station the powder will then be presented to other instruments for performing a detailed chemistry, physical, and spectral analyses.

1.2.2 The ExoMars Rover Instrument Suite Looking for signatures of life on Mars

An accurate visual and spectral characterization of the surface of Mars is fundamental to establish the geological context at the sites that the Rover will visit. This can be complemented by electromagnetic and neutron subsurface investigations, which will further contribute to understand the depositional environment (e.g. sedimentary, volcanic, Aeolic). Knowledge of the geological history of past water environments constitutes a necessary step in the search for traces of past or present signatures of life on Mars.

Data from the novel suite of instruments on-board the ExoMars rover will help scientists to conduct a step-by-step exploration of Mars, beginning

at panoramic (meter) scales and progressively converging to smaller (sub-millimeter) studies, concluding with the molecular identification of organic compounds.

Instruments in brief

- PanCam - The Panoramic Camera To perform digital terrain mapping of Mars.
- ISEM - Infrared Spectrometer for ExoMars To assess the mineralogical composition of surface targets. Working with PanCam, ISEM will contribute to the selection of suitable samples for further analysis by the other instruments.
- CLUPI - Close - UP Imager A camera system to acquire high-resolution color close-up images of rocks, outcrops, drill fines and drill core samples.
- WISDOM - Water Ice and Subsurface Deposit Observation On Mars A ground-penetrating radar to characterize the stratigraphy under the rover. WISDOM will be used with Adron, which can provide information on subsurface water content, to decide where to collect subsurface samples for analysis.
- Adron To search for subsurface water and hydrated minerals. Adron will be used in combination with WISDOM to study the subsurface beneath the rover and to search for suitable areas for drilling and sample collection.
- Ma_MISS - Mars Multispectral Imager for Subsurface Studies Located inside the drill, Ma_MISS will contribute to the study of the Martian mineralogy and rock formation.
- MicrOmega A visible plus infrared imaging spectrometer for mineralogy studies on Martian samples.
- RLS - Raman Spectrometer To establish mineralogical composition and identify organic pigments.
- MOMA – Mars Organic Molecule Analyzer MOMA will target biomarkers to answer questions related to the potential origin, evolution and distribution of life on Mars. [18]

1.3 Mars

Mars (Figure 8) is the fourth planet from the sun and the next planet beyond Earth. It is, on average, more than 142 million miles from the sun. Mars is about one-sixth the size of Earth. Mars is known as the Red Planet (Table 1). It gets its red color from the iron oxide (like rust) in its soil.

Mars is named for the ancient Roman god of war. The Greeks called the planet Ares. The Romans and Greeks associated the planet with war because its color resembles the color of blood.

Mars has two small moons. Their names are Phobos and Deimos. They are named for the sons of Ares, the Greek god of war. Phobos means "fear," and Deimos means "flight."[12]

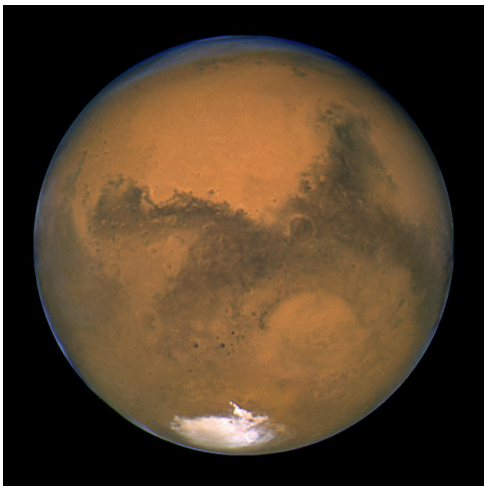

Figure 8: Hubble's close encounter with Mars
Picture taken from[19]

1.3.1 Internal structure

Like Earth, this planet has undergone differentiation, resulting in a dense, metallic core region overlaid by less dense materials. Current models of the planet's interior imply a core region about 1,794 km (1,115 mi) ± 65 km (40 mi) in radius, consisting primarily of iron and nickel with about 16–17% sulfur. This iron sulfide core is partially fluid, and has twice the concentration of the lighter elements that exist at Earth's core. The core is surrounded by a

Bulk facts	Earth	Mars
Average Distance from Sun	93 million miles	142 million miles
Average Speed in Orbiting Sun	18.5 miles per second	14.5 miles per second
Diameter	7,926 miles	4,220 miles
Tilt of Axis	23.5 degrees	25 degrees
Length of Year	365.25 Days	687 Earth Days
Length of Day	23 hours 56 minutes	24 hours 37 minutes
Gravity	9.81m/s^2	3.75m/s^2
Temperature	Average 287 degrees K	Average 210 degrees K
Atmosphere	nitrogen, oxygen, argon, others	mostly carbon dioxide, some water vapor
Number of Moons	1	2

Table 1: Mars bulk facts
Taken from [19]

silicate mantle that formed many of the tectonic and volcanic features on the planet, but now appears to be dormant. Besides silicon and oxygen, the most abundant elements in the Martian crust are iron, magnesium, aluminum, calcium, and potassium. The average thickness of the planet's crust is about 50 km (31 mi), with a maximum thickness of 125 km (78 mi). Earth's crust, averaging 40 km (25 mi), is only one third as thick as Mars's crust, relative to the sizes of the two planets. The InSight lander planned for 2016 will use a seismometer to better constrain the models of the interior.[26]

1.3.2 Mars seasons

Mars has one of the highest orbital eccentricities of any planet in our solar system (other than Mercury and Pluto) – its distance from the Sun varies between 1.38 and 1.67 AU over the Martian year. This large variation, combined with an axial tilt slightly greater than Earth's, gives rise to seasonal changes far greater than we experience here on Earth. On Mars, dramatic dust storms are common due to solar heat, which warms the Martian atmosphere and causes its air to move rapidly, lifting dust off the ground. Because the Martian atmosphere is thin – about 1% as dense as Earth's at sea level – only the smallest dust grains hang in the air, and the grains are as fine as smoke. One of the strangest effects of seasons on Mars is the change in atmospheric pressure. During winter the global atmospheric pressure on Mars is

25% lower than during summer. This happens because of the eccentricity of Mars's orbit and a complex exchange of carbon dioxide between the Martian dry-ice polar caps and its CO2 atmosphere. Around the winter solstice when the North Pole is tilted away from the sun, the northern polar cap expands as carbon dioxide in the polar atmosphere freezes. At the other end of the planet the southern polar cap melts, giving CO2 back to the atmosphere. This process reverses half a year later at the summer solstice. But Mars is 10% closer to the Sun in southern summer than it is in northern summer. At the time of the winter solstice the northern polar cap absorbs less CO2 than the southern polar cap absorbs half a year later. The difference is so great that Mars's atmosphere is noticeably thicker during northern winter. Its orbital motion is slowest when it is at aphelion (the farthest point from the Sun) and fastest at perihelion (the closest point to the Sun). This makes Martian seasons vary greatly in duration than those on Earth. Seasons change roughly every six months, with northern spring and fall lasting 171 Earth days, northern summer being 199 days in length, and northern winter being only 146 days. Because of these variations, Martian seasons do not start at the same Earth day each Martian year.[11]

1.3.3 Martian Atmosphere

The global Martian atmosphere dynamics are ruled by the Hadley circulation (Figure 9), the warmer air raises at equator, cools at higher altitudes, flows towards the poles and closes the circulation towards the equator and meridional (SouthNorth) movements (Table 2).The Coriolis effect (generated by planet's rotation) causes strong lateral zonal winds (East-West), and a large Hadley cell forms, involving both hemispheres and straddling the equator, and the vertical movements are not prevented due to the lack of a stratosphere.[5]

1.3.4 Martian dust

Martian dust comes from clastic alteration, chemical weathering and erosion (wind/water/ice) of rock beds, as well as regolith (impacts of all sizes), dust is permanently present in the atmosphere with variable abundance, it is a key role in the dynamic and thermodynamic evolution of the atmosphere (large scale circulation at diurnal-seasonal-annual time-scales)(Figure 10). Wind effects on dust at various scales like dust cycle, dust storms and dust devils

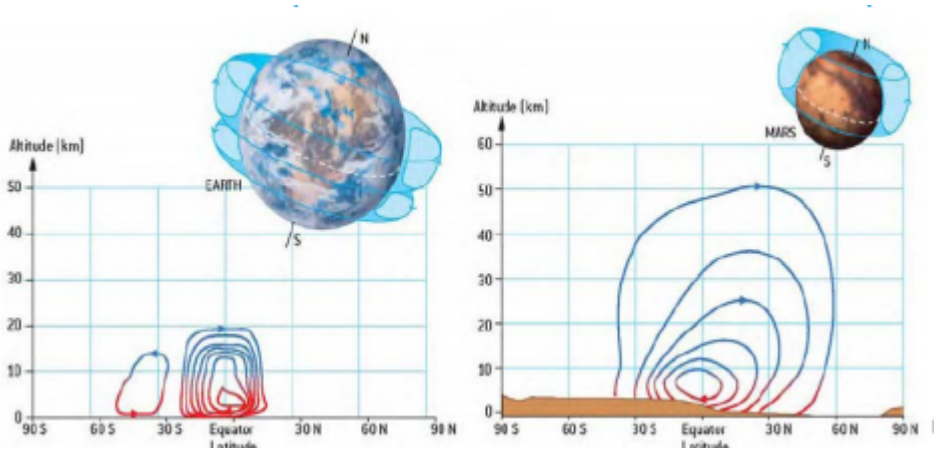

Figure 9: Meridional winds and Hadley circulation on Earth and on Mars
Picture taken from[8]

Atmospheric Parameters	
Composition (volume fraction)	95.32% CO 2, 2.70% N2, 1.60% Ar40, 0.13% O2, 0.07% CO, 0.03% H2O, 0.013% NO, 5.3 ppm Ar36+38, 2.5 ppm Ne, 0.3 ppm Kr, 0.13 ppm CH 2O, 0.08 ppm Xe, 0.04-0.02 ppm O3, 10.5 ppb CH4
Mean Molecular Mass	43.49 g/mole
Pressure	6.1 mbar (average) - 0.2-12 mbar (range)
Temperature	215 K (average) - 140-310 K (range)
Wind Speed	0-30 m/s
Atmospheric visible optical depth	0.1-10 [0.1-0.3 under clear conditions]
Atmospheric dust mass density	1-100·103 kg/m3 [if $\geq$1 increased dust];
Atmospheric dust particle number density	1-100 cm-3 [if >5 major dust storm]
Atmospheric dust grain size	0.010-10 μm

Table 2: Martian atmosphere
Taken from [5]

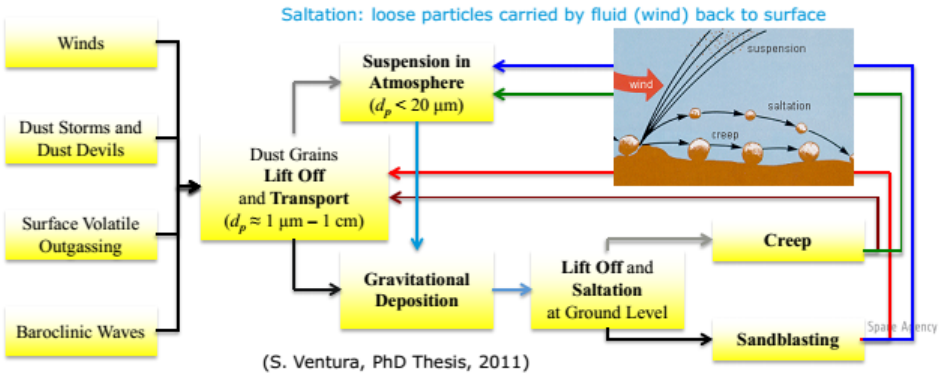

Figure 10: Dust in Mars
Picture taken from [5]

are typical phenomena involving atmospheric dust.

The dust cycle is characterized by lifting, transport in the atmosphere, deposition and eventual scavenging by clouds and precipitation. Winds cause grains (size ~ 1 µm - 1 cm) to lift off from surface. The smaller particles (dp $< 10\mu m$) go in suspension in the atmosphere, while the larger ones are lifted but do not go in suspension carried down by winds to surface, where they bounce back into flight (saltation). Average saltation trajectories are about 1 m long and 10-20 cm high. Saltating sand and grains may strike larger grains (dp $<$ 1 cm) and push them along the surface (creep). Saltation may also trigger the injection of much smaller particles (suspension) impacts. The physical boundary between the saltation and suspension phenomena is not well defined, so, commonly, it is assumed that particles with settling velocity quite lower than the threshold friction velocity are ruled by suspension, while particles with settling velocity higher than the threshold friction velocity are ruled by saltation. Sandsized aggregated particles can be raised and then broken down into much smaller particles by collisions (sandblasting). Finally, surface volatile outgassing, dust storms and dust devils, and planetary baroclinic waves are also responsible of injection and transport of particles in the atmosphere.[27]

1.4 Instrumentation

1.4.1 Medusa

The MEDUSA experiment (Table 3) accommodates a complement of sensors that have been conceived in order to provide a full set of quantitative in-situ information about cumulative dust mass flux and dust deposition rate, dust physical and electrification properties, size distribution of sampled particles and water vapour abundance versus time. The MEDUSA experiment is formed by four main sub-systems :

- The MEDUSA main body, including a sampling head, an optical detection stage (OS), a dust collection stage based on a quartz crystal microbalance (MBd) and a pumping system.
- The dust deposition and electrification sensor (DDES).
- The water vapour detection sensor based on a Peltier conditioned quartz crystal microbalance (MBw).
- The main electronics (ME) controlling the sensors functioning and commanding and telecommand (TC) and telemetry (TM) exchange with the ExoMars main system electronics.

The MEDUSA main body foresees the use of an active sampling system to drag the Mars atmospheric gas, carrying the dust particles, through the instrument to allow the monitoring of particles by the OS and the following dust collection stage (MBd). The OS is accommodated inside a cylinder-shaped case on the top side of the instrument and couples forward (angles 6–301) and backward (angles 135–170) scattering detection in dark field for each particle (particle counting). Coupling the two signals will give information on the particle optical constants, as the backscattered radiation amplitude is relatively more dependent on the refractive index than the forward component. A laser diode source provides illumination when the particle passes through the sampling volume. The output beam is collimated by a refractive optical system in order to confine the OS sampling volume (3 mm x3 mm x 0.1 mm). Two mirrors are used to collect the forward and the backward scattered lights and concentrate them on two photo-detectors. A light trap collects the “direct” laser beam after its focus. The MBd is used as collection stage under the OS to measure the collected cumulative dust mass.

Sub system	Measured quantity	sensitivity	saturation
Optical detection stage (OS)	Single particle size (μm)	0.2	100
Single particle size (mm) 0.2 100 Optical detection stage (OS)	Particle number density (cm3)	$\ll 1$	500
Microbalance for dust (MBd)	Cumulative mass of dust (kg)	$2x10^{-13}$	$2x1^{-9}$
Microbalance for water vapour (MBw)	Water vapour abundance (ppb)	1	saturation in atmosphere
Dust deposition and electrification sensor (DDES)a	Dust deposition (%)	1	100
Dust deposition and electrification sensor (DDES)	Electrification (e)	10^3	10^6
Dust deposition and electrification sensor (DDES)	Wind speed (m s1)	2	20

Table 3: Performances of MEDUSA sub-systems
Table taken from [6]

We recall that quartz crystal micro-balances (MBs) are based on piezo-electric transducers, that give an output signal whose frequency is proportional to the mass deposited on the sensor. The measured physical quantity is the shift of the resonant frequency of a quartz oscillator. As MBs are sensitive to the total deposited mass, they are well suited to measure the mass of micron/sub-micron particles. Actually, the sensitivity of MBs to micron/sub-micron particles has been tested in previous laboratory experiments.

A driving aspect in the MEDUSA design is the fluid dynamic design inside the OS and MBd sub-systems. In fact, the efficient collection of dust depends on the proper sizing of the external and internal mechanical elements, in particular the sampling head and the size of the nozzle of the collection stage, the distance of the impact plate from the nozzle and the overall internal dimensions of the stage (to minimize undesirable turbulent effects).

The water vapour MBw sensor is protected by a case to avoid dust contamination and direct illumination by solar radiation; the configuration of the aperture, allowing free access to the environmental water vapour to be monitored, is below the sensor itself to exclude contamination by dust set-

tling on the sensor. The DDES constitutes an integration of three sensors: a dust deposition and passive removal sensor, a dust electrification sensor and a laser anemometer.

Dust deposition is accurately quantified at six places on the instrument by detecting laser light scattered into photo-detectors. Moreover, electric fields are applied to a dust accumulator surface using a variable highvoltage source and transparent electrodes made by vapour deposition of indium oxide. Both positive and negative electrodes are used in order to determine the fraction and degree of electrification of the dust. Patterned laser beams are created using holographically generated interference gratings. Each single particle crossing the pattern generates a time-varying light back-scattered signal which is collected using a Fresnel lens and detected using a photodiode. This quantifies the wind velocity, while the detection rate measures the suspended dust concentration.

Finally, the ME board(s) dedicated to the management of the MEDUSA experiment is (are) allocated in a box common to the whole system. The ME (or Data Processing Unit) of MEDUSA will be the electrical interface of the instrument to the system. The ME will include also power conversion and conditioning to satisfy MEDUSA needs.

The MEDUSA onboard software will process the TCs sent in raw format following a standardised data structure and protocol. A set of HK parameters (including operative and not operative limits) will be defined to be monitored (high level) by the onboard software. The low level monitoring will be done by the MEDUSA software. If one of the parameters runs out of limits, then the MEDUSA software will start a predefined set of high level recovery actions. MEDUSA will run in a predefined set of operative modes. For each mode, it shall be defined: actions to be taken before going into the operative mode, accepted/rejected TC, generated TM, peak and average data rate, resources consuming (e.g., CPU, memory, power), valid/invalid mode transition, actions to be taken before exiting the mode.

In order to achieve scientific objectives, the MEDUSA main body (including the inlet, OS and MBd sensing systems) shall protrude from the mounting platform vertically, with the sampling head exposed to atmosphere, in order to have as much as possible free space all around the sampling head and shall have unobstructed field of view horizontally around its sampling head. Similarly, the DDES shall be exposed to atmosphere, to have free space above its upper surface and as much as possible free space all around it, to minimise air flow perturbation. Finally, the MBw needs a good thermal contact with

system structure, at temperature close to the atmospheric one and shall be exposed to external atmosphere to allow unbiased sampling of water vapour.

In particular, MEDUSA shall measure the size of atmospheric dust in the wide size range of interest (from 0.05 to 10 mm); it shall be possible to detect optically single particles $\geqq$0.1 mm in radius and to measure the cumulative mass of smaller grains. A statistical analysis of the results obtained in a typical run of the instrument shall provide the actual atmospheric dust size distribution.

The measurement of the particles number density versus size is related to the previous result through the sampling operations. Once particle counting and/or mass measurements have been performed, dust number density can be derived, since the volume sampled by the system is known. From the operational point of view this requires a careful control of the atmospheric volume.[6]

1.4.2 MicroMed

The concept of MicroMed (Table 4) was developed when ESA established to replain the ExoMars lander mission into the Entry, Descent and Landing Demonstrator Module (EDM) 2016 mission. MicroMed, a MEDUSA miniaturization, was conceived in order to satisfy the imposed stringent limitations in terms of mass, accommodation and power consumption. MicroMed was included into the DREAMS (Dust Characterisation, Risk Assessment, and Environment Analyzer on the Martian Surface), a scientific package proposed in response to the ESA Announcement of Opportunity for the EDM science payload. The DREAMS package has been selected by ESANASA for the ExoMars EDM 2016 in June 2011, but the adopted configuration not including MicroMed. Nevertheless, the MicroMed study has been carried on for next Mars exploration opportunities.[27]

The MicroMed optical design is driven by the following requirements:

- To concentrate the laser beam in a small area in order to obtain high power density with a low power laser
- To be able to detect particles in the size range 0.4 – 20 μm in diameter
- To be able to detect single particles (having a small fraction of coincidence f (e.g. < 0.05))
- To maximize the power density in the sampling volume

	MEDUSA	MicroMed
Total Mass	2243 g	500 g (without ME) (TBC)
Total Maximum Power Consumption	21.44 W	1.6 W (only PE)
Sampling Head	Nozzle	Minimized tube
Collecting mirrors aperture	±33° in FW direction ±47° in BW direction	1 mm x 1 mm x 0.08 mm
Sampling Volume	1.2 mm x 0.32 mm x 3 mm	±65° at 90° direction
Detector(s)	Sensing Area: 50 mm2 Responsivity: 0.5 A/W	Sensitivity Area: 50 mm2 Responsivity: 0.5 A/W
Laser Diode	Wavelength: 808 nm Optical Power: 1000 mW	Wavelenght: 850 nm Optical Power: 100 mW
Pump	Maximum Flow Rate: 5.5 l/min	Maximum Flow Rate: 1.0 l/min
Microbalance for dust	Mass Sensitivity: 5.09·108 Hz/g/cm2	NO
Microbalance for water vapour	Mass Sensitivity: 2.47·109 Hz/g/cm2	NO
Proximity Electronics	4 Channels (2 for Forward Scattering + 2 for Backward Scattering)	1 Channel with 2 outputs: low gain 105, high gain 107

Table 4: MEDUSA vs MicroMed
Taken from[7]

- To produce a beam with uniform intensity inside the sampling volume (in order to avoid that the same particle could produce different signal if intercepting the beam in different points)

1.5 Objectives

The main objectives of this work are the mechanical and fluid dynamics assessment of an inertial filter capable of preventing the capture of particles with diameter higher than $20-30\mu m$, because this coarser particles can block the pumping system of the instrument.

With the CFD design the mass of the overall system can be reduced due to the optimization of the length of the inlet and the pipeline to the optical stage, the design of both the inlet and the transport system has to minimize the loss of the sample particles keeping them intact to the region, where they should be examined.

2 Computational fluid dynamics (CFD) design of the inertial filter

2.1 Inertial classifiers

The principle of inertial classification of particles uses the particle's inertia for their classification. Classification is achieved in these instruments by turning the gas flow and capturing the particles with sufficient inertia to cross gas streamlines and escape the flow. Particles with lower inertia will remain in the gas flow.

There are four types of inertial clasifiers

- The body impactor (Figure 11.a), is the simplest, consists of only a body in a moving aerosol stream onto which particles impact. The latter three of the inertial classifiers all consist of a jet of gas impinging on a target.

- A conventional impactor (Figure 11.b), in its simplest form, consists of a jet of particle-laden gas impinging on a flat plate with particles impacting on the plate. Variations of the impactor include the use of either round or rectangular nozzles, single or multiple nozzles, and flat or cylindrical impaction plates.

- In a virtual impactor (Figure 11.c), the impaction plate is replaced by a collection probe slightly larger than the nozzle, with the classified particles penetrating into the collection probe. A small fraction of the gas passes through the collection probe to transport the classified particles out the lower end of the probe. The remained of the gas, the major portion, reverses direction in the collection probe and escapes at the upper edge.

- In the cyclone (Figure 11.d), the aerosol stream is drawn through the inlet and impinges tangentially on the inner surface of a cylinder, flows in a spiral pattern down the inside of the cylinder and cone walls, reverses direction, spirals upward around the cyclone axis, and exits through a centrally located tube at the upper end of the cylinder. Particles are collected on the cylindrical and conical walls by inertial forces on the particles. Clumps of impacted particles that are knocked off or dropped from the cyclone walls tend to fall to the apex of the cone

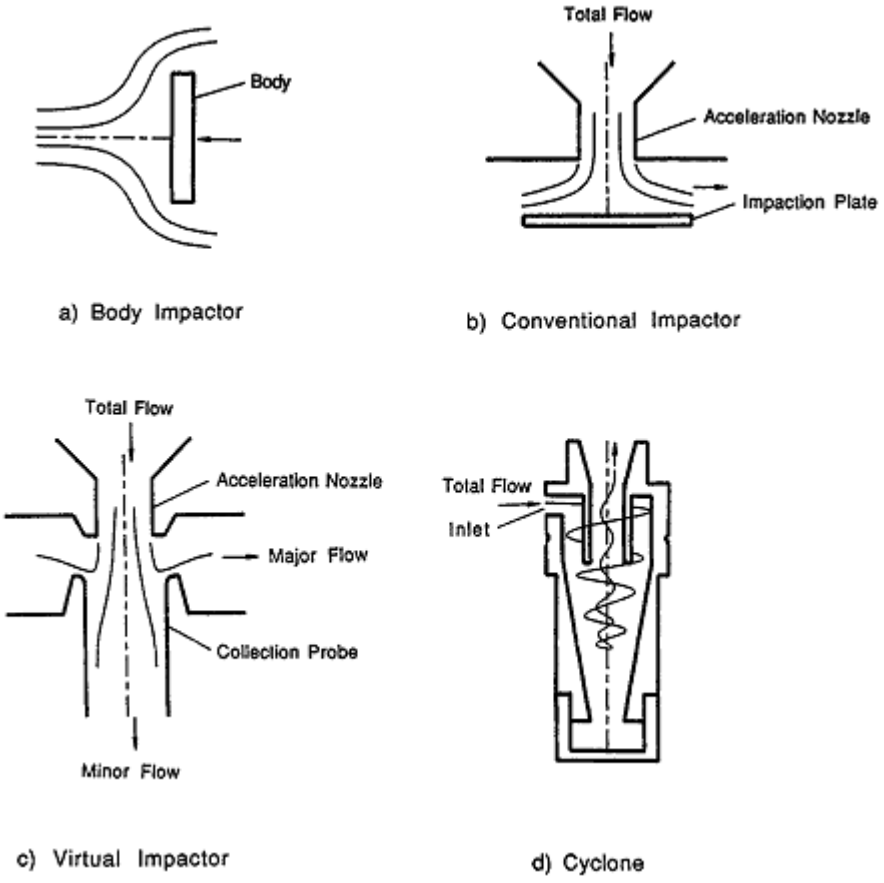

Figure 11: Four types of inertial classifiers
Picture taken from [21]

where they are collected in a cup, sometimes called a dust cap or grit pot.

The simplest type of inertial classifier is a body collector, which is a body (usually cylinder or ribbon) passing through particle-laden gas. As this body moves through the gas, the gas is deflected around the body. Large particles, however, due to their inertia, are not deflected as much as small particles and will strike the surface of the body.

The velocity of the air,U,the size of the particle, d_p, and the size of the body, d_b, are three important parameters in determining whether or not a particle will be collected on the body. A dimensionless parameter, the Stokes number, which could be interpreted as the ratio of the particle's stopping distance to the physical dimension of the body collector, is the governing relationship as to whether or not a particle will strike the body. The Stokes number, Stk, is defined as

$$Stk = \frac{\rho_p C_c d_p^2 U}{18 \mu d_b} \tag{1}$$

where
ρ_p =Particle density
C_c = Cunninghanm slip correction
U = Relative velocity of body to gas
d_p =Particle diameter
μ = Gas viscosity
d_b = Body diameter

The Stokes number is important in all types of inertial collectors and not just body collectors. The Stokes number for a conventional impactor or a virtual impactor is the ratio of the stopping distance to the radius of a circular nozzle, or half width of a rectangular nozzle, and it is defined as

$$Stk = \frac{\rho_p C_c d_p^2 U}{9 \mu W} \tag{2}$$

where
U =Average gas velocity at the nozzle exit $=Q/\pi(W/2)^2$(round nozzle impactor) or $=Q/LW$ (rectangular nozzle impactor)
W =Nozzle diameter (circular impactor) or nozzle width (rectangular impactor)

Q =Volumetric flow rate through the nozzle
L =Rectangular nozzle length

The Stokes number is a dimensionless parameter that can be used to predict whether or not a particle will impact on a body, an impaction plate or in the collection probe of a virtual impactor, or it will follow the air streamlines out of the impaction region and remain airborne. Actually, the square root of Stokes number, $\sqrt{Stk}$, is more commonly used because it is can be represented as a dimensionless particle size. A critical value of $\sqrt{Stk}$, often used to characterize inertial classifiers, is $\sqrt{Stk_{50}}$. This is the value of $\sqrt{Stk}$ corresponding to d_{50},the value of d_p at which particles are collected with 50% efficiency. Thus, if the value of$\sqrt{Stk_{50}}$ is known, the value of d_{50},corresponding to the cut size of the impactor, can be found from.

$$d_{50} = \sqrt{\frac{18\mu d_b}{\rho_p C_c U}}\sqrt{Stk_{50}} \tag{3}$$

for body impactors, and

$$d_{50} = \sqrt{\frac{9\mu W}{\rho_p C_c U}}\sqrt{Stk_{50}} \tag{4}$$

for conventional and virtual impactors.

2.1.1 Body Impactors.

The body impactor (Figure 11.a) works by sweeping an impaction surface (body) through the air or, instead air pass the body. In either cases, the problems associated with the sampling of large particles is reduced.

The collection efficiency of the body impactor is defined as the fraction of particles that are impacted on the body from a volume of air swept out by the body . Particle collection curves are presented for particle deposition on ribbons, spheres, and cylinders. The cut size is a function of the body size (dimension normal to the flow direction) and the relative velocity between the air and body.The cut size is governed by the Stokes number equation where d_b is the body size and U is the velocity difference between the air and the body.

The importance of the jet Reynolds number is more related to the sharpness of cut than to the cut size of the impactor. If the Reynolds number

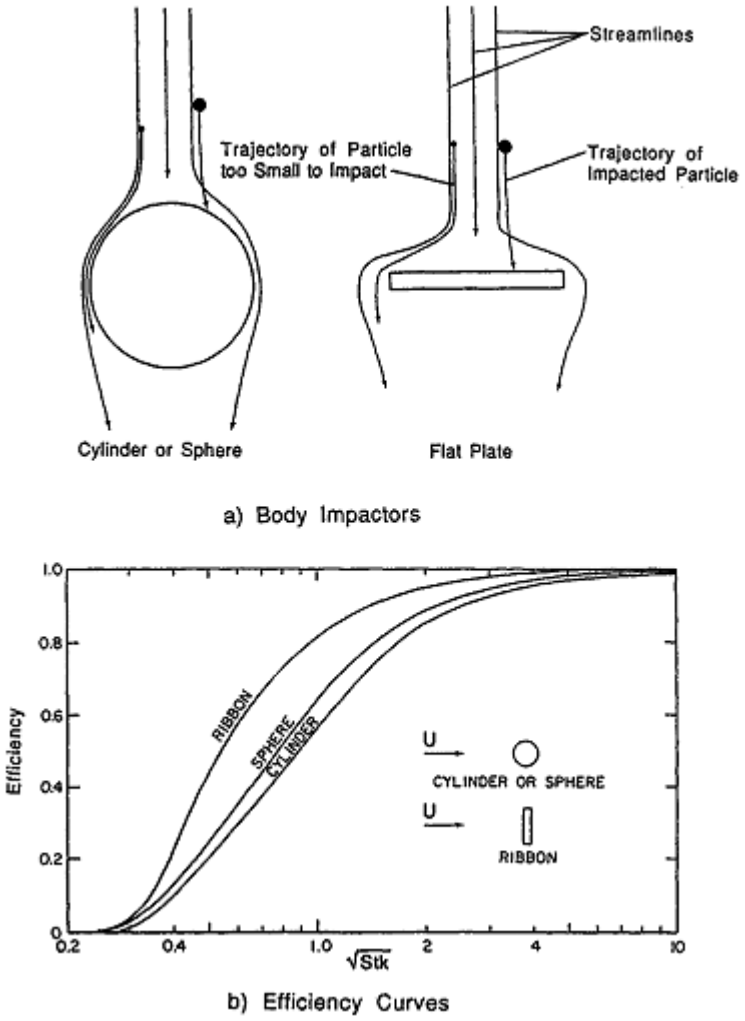

Figure 12: Schematic diagrams of body impactors and corresponding particle collection efficiency curves from Golovin and Putnam (1962)
Picture taken from [21]

is low, the gas viscous forces will be large and the velocity profile will be parabolic at the nozzle exit and in the air jet as it approaches the impaction plate. This will enhance the collection of particles near the center line, where the smallest particles will be collected. The low velocity near the nozzle wall will require the particles in this portion of the flow to be larger in order for collection to occur. Therefore, the result of an impactor operating at a low Reynolds number is a less sharp collection efficiency curve. Theoretical analysis has shown, and experiments have verified, that the efficiency curve will be its sharpest if the Reynolds number is kept in the 500 to 3000 range for both round and rectangular impactors.

$$Re_j = \frac{\rho_f W U}{\mu} \tag{5}$$

Round

$$Re_j = \frac{2\rho_f W U}{\mu} \tag{6}$$

Rectangular

2.2 Characterization of dispersed solid-liquid flows

The two-phase flows considered in this thesis are referred to as dispersed because one phase (the solid) is present in the form of particles dispersed in a continuous carrier phase (the liquid).

The most common way of performing an hydrodynamic characterization of dispersed solid-liquid flows, is to make reference to integral properties (Figure 14). The most important property is particle concentration, which is defined as the volume fraction of particles, i.e. the ratio between the volume of particles in a local volume of mixture and the volume of mixture itself.. The volume fraction of the dispersed phase α_p is :

$$\alpha_p = \frac{\sum_i N_i V_{pi}}{V} \tag{7}$$

where V is the total volume and N_i is the number of particles of size$i$, having volume V_{pi} , $V_{pi} = \pi d_{pi}^3/6$, where d_{pi} is the particle diameter in case of spherical particles, or their volume-equivalent diameter of a sphere elsewhere.

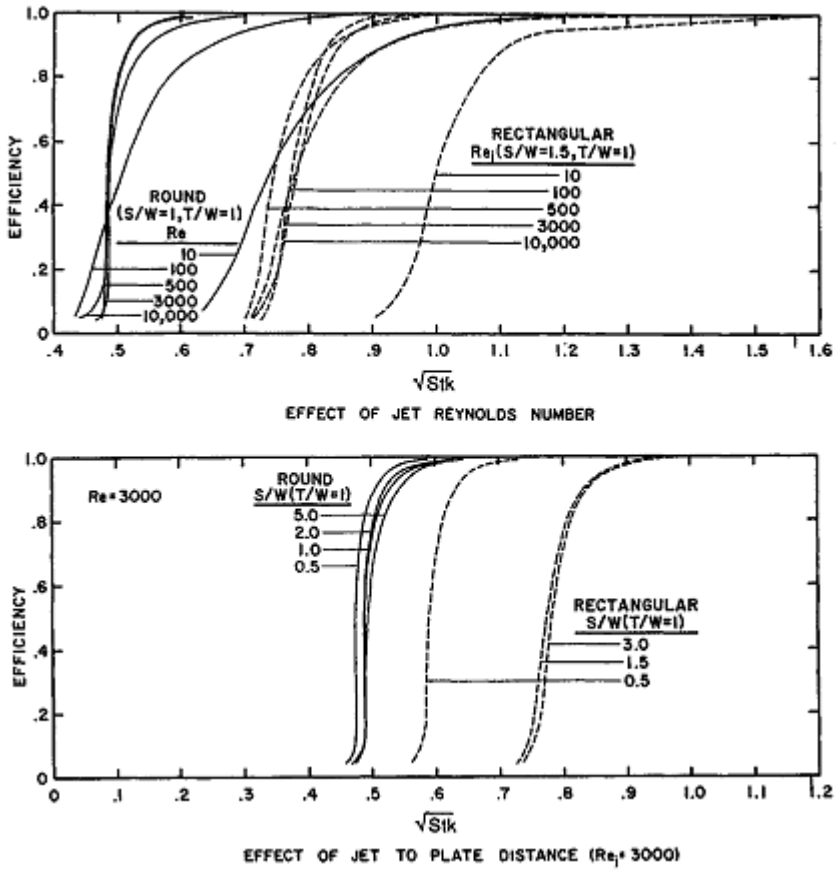

Figure 13: Theoretical impactor efficiency for rectangular and round jet impactors showing the effect of jet-to-plate distance ratio (S/W) an jet Reynolds number (Re_j)

Picture taken from [21]

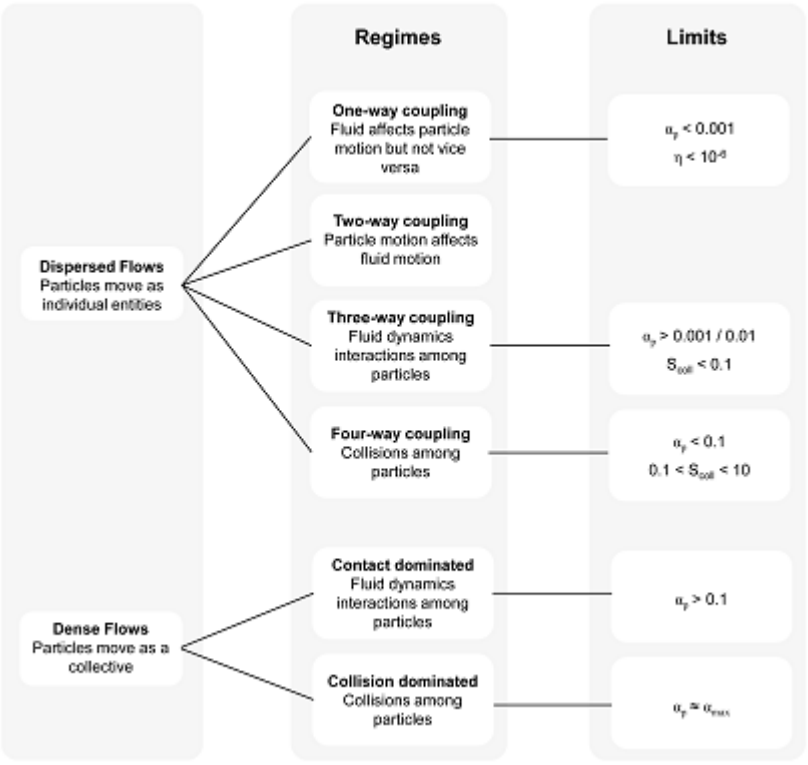

Figure 14: flow regimens and limits reported in the literature
Picture taken from [10]

Since the sum of the volume fraction of the dispersed phase and the carrier phase is unity, the volume fraction of the carrier fluid is:

$$\alpha_f = 1 - \alpha_p \tag{8}$$

Other definitions for particle concentration have been proposed. For example, the mass loading η is the ratio between the mass of the particles to that of the fluid in a local volume of mixture:

$$\eta = \frac{\alpha_p \rho_p}{(1 - \alpha_p)\rho_f} \tag{9}$$

beingρ_p and ρ_f the density of the particles and the fluid respectively.

The integral properties define above affect the kind of interaction between the two phases in the flow (couple regimes) and therefore, the different ways

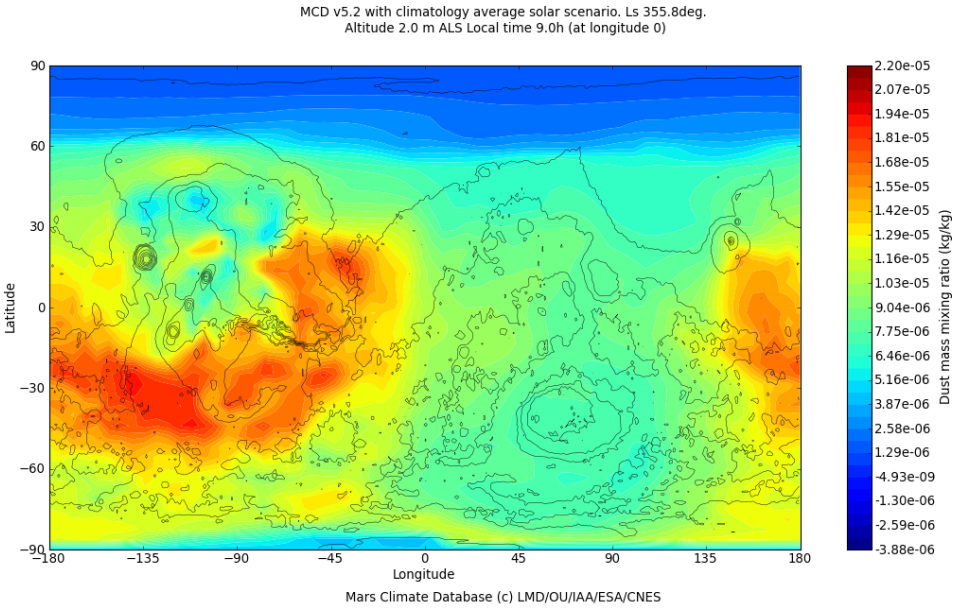

Figure 15: Mass loading in the climatology average solar scenario
Picture take from[22]

to approach the problem of the two-phase flow modeling.

In the Martian atmosphere the maximum mass loading in a dust storm is $\eta \approx 4.5^{-4}$, in average conditions the maximum mass loading (Figure 15) $\eta \approx 2.2^{-5}$ and the average $\eta \approx 1.06^{-5}$[22].

According to this values the assumption of *One-Coupling* regime is satisfied, The assumptions of this regime are that the particle motion is affected by the fluid but not vice-versa, however, it is typically assumed that the *One-Way coupling regime* occurs for $\alpha_p \ll 1$ or $\eta \ll 1$ (Figure 14). Guidelines reported in literature are $\eta < 10^{-3}$ and $\alpha_p < 10^{-6}$ [10].

2.3 Particle size distribution on Mars atmosphere

The particle size distribution of a given dust or mist can be reported as a number, length, surface, volume or mass (weight) distribution. The curves in the Figure 16 are density curves: the function values $f(x)$ represent the fraction of particles in a given interval divided by the width of that interval. The definition of the number density distribution $f_N(x)$ is thus:

$f_N(x)dx$ = the number fraction of particles with a diameter between x −

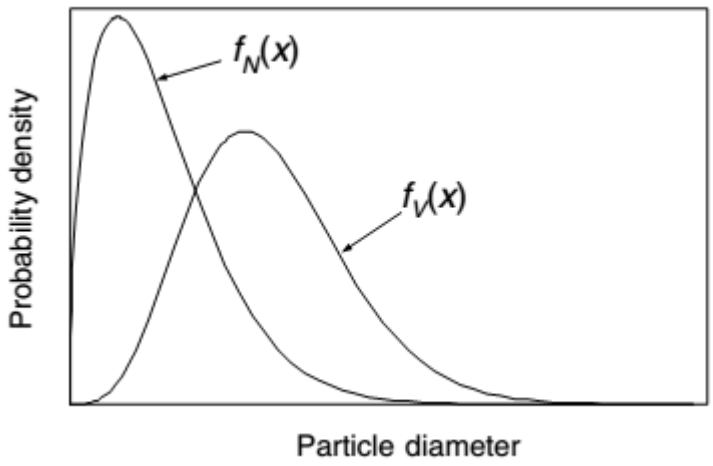

Figure 16: Number and volume density distribution for sample powder
Picture taken from[3]

1/2 dx and x + 1/2 dx,

and the definition of the volume density distribution $f_V(x)$ is:

$f_V(x)dx$= the volume fraction of particles with a diameter between x − 1/2 dx and x + 1/2 dx, which is related to the previous distribution by Equation 10.

Since the particle volume is proportional to x^3, the larger particles contribute much more to the volume distribution than to the number distribution. This can be seen in the shapes of the curves. The larger particles contribute negligibly to the number distribution, which appears to go to zero, while they contribute substantially to the volume distribution.[3]

$$f_V(x)dx = \frac{\frac{\pi x^3}{6} fN(x)dx}{\int_0^\infty \frac{\pi x^3}{6} fN(x)dx} \tag{10}$$

In addition to density distributions, a very widely used method of reporting a particle size distribution is through the use of its 'cumulative undersize distribution' $F(x)$ see Figure 17, defined as the fraction of particles with a diameter less than x. $F(x)$ is related to the density function $f(x)$ by:

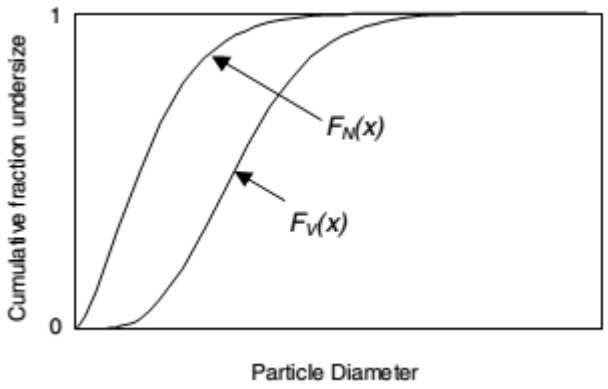

Figure 17

Figure 17: Cumulative number and volume distribution for powder
Picture taken from[3]

$$F(x) = \int_0^x f(z)dz \qquad f(x)dx = dF(x) \tag{11}$$

where z is the dummy variable of integration.

The particle size distribution on the martian atmosphere change due to the zone in the planet and the height in which you are interested in, you can represent this distribution with a modified gamma distribution.

$$N(r,z)/C = (r/a(z))^{(1-3b(z))/b(z)} exp(-r/(a(z)b(z))) \tag{12}$$

In this formula is $a(z)$ equal to the mean radius, $b(z)$ is and spread factor, r equal to the radius of the particles, z the height, C has the same dimensions as $N(r)$ and will be used as a normalizing factor, which can in principle be adjusted to provide results appropriate to a specified optical depth and $N(r)$ is the number of particles of radius r .

The dust is initially mixed uniformly to 10 km but then slowly settles out while being mixed through the boundary layer by turbulence. Then the surface friction velocity, exceeds the threshold value (1.3 m s−1) around the middle of the sol (0930–1400), so that the surface acts as second source of dust particles. This sources of dust crate a cycle over the sol, mixing the atmospheric layer of Mars generating different dust distributions depending of the high an the place in the planet (Figure 18).

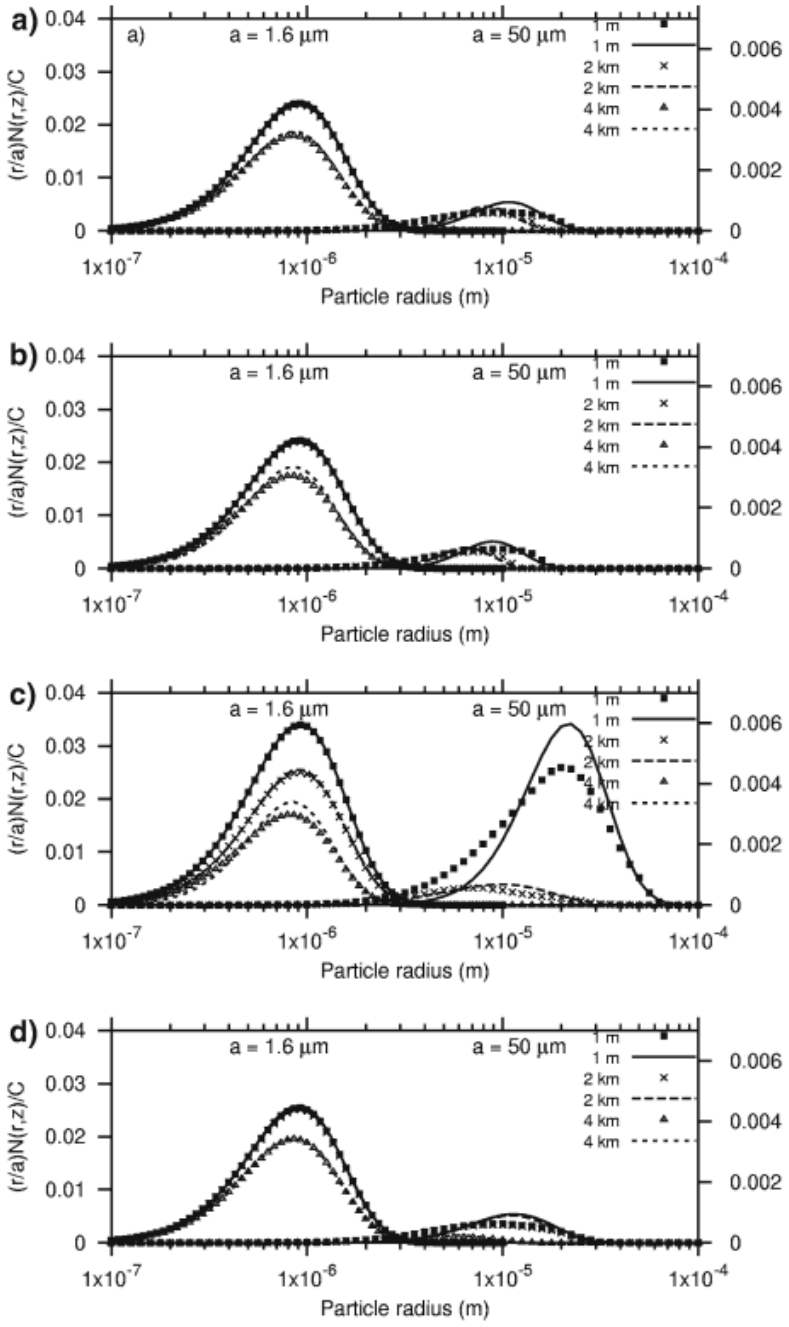

Figure 18: Normalised particle size distributions at different altitudes. Symbols: $N(r,z)/C$ obtained from model predictions; lines: Gamma distributions computed from cross-section-weighted radius a(z), cross-section-weighted variance (normalised by a^2) b(z) and good-fitted values c(z). (a) at 0000; (b) at 0600; (c) at 1200; (d) at 1800 (Mars hours)

Picture taken from[9]

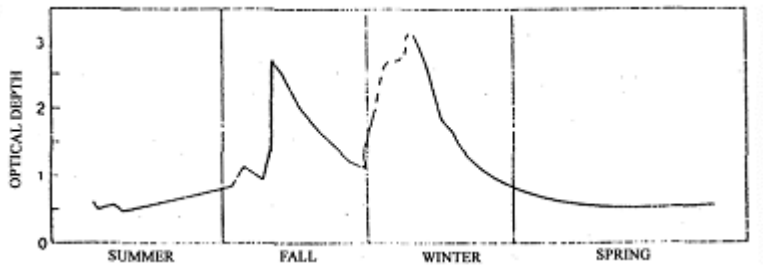

Figure 19: Atmospheric optical depth in a martian year
Picture taken from[27]

This two sources of dust can be modeled by two modified gamma distributions at a height of one meter, for the first one $b = 0.2$, as mean radius $a = 1.6\mu m$, for the second one a much coarser dust whit $a = 50\mu m$ and $b = 0.2$.[9]

Dust scattering is the most important attenuation process in the Martian atmosphere. The extinction coefficient at optical wavelength λ due to , $\sigma_\lambda(m-1)$ can be modeled as,

$$\sigma_\lambda = \int_0^\infty N(r,z) b_{r,\lambda} dr \tag{13}$$

where $b_{r,\lambda}$ is the effective scattering cross-section of a single aerosol of radius r. For spherical dust particles, the effective scattering cross-section for a single particle is given by

$$b_{r,\lambda} = \pi r^2 Q_{r,\lambda} \tag{14}$$

where $\pi r^2$is the actual dust particle cross-sectional area, and $Q_{r,\lambda}$(dimensionless) is the . The scattering efficiency is a function of a complex index of refraction, wavelength of the light and a size parameter.

The extinction inefficiencies $Q_{ext} = Q_{r,\lambda}$ for Martian dust, indicate variation from about 2.8 at $500nm$ to 3.3 at $1,000nm$, no dependence on particle size is indicated.

Optical depth (dimensionless) () quantifies the scattering and absorption that occurs between the top of the atmosphere and a given altitude, zlb, and is given by

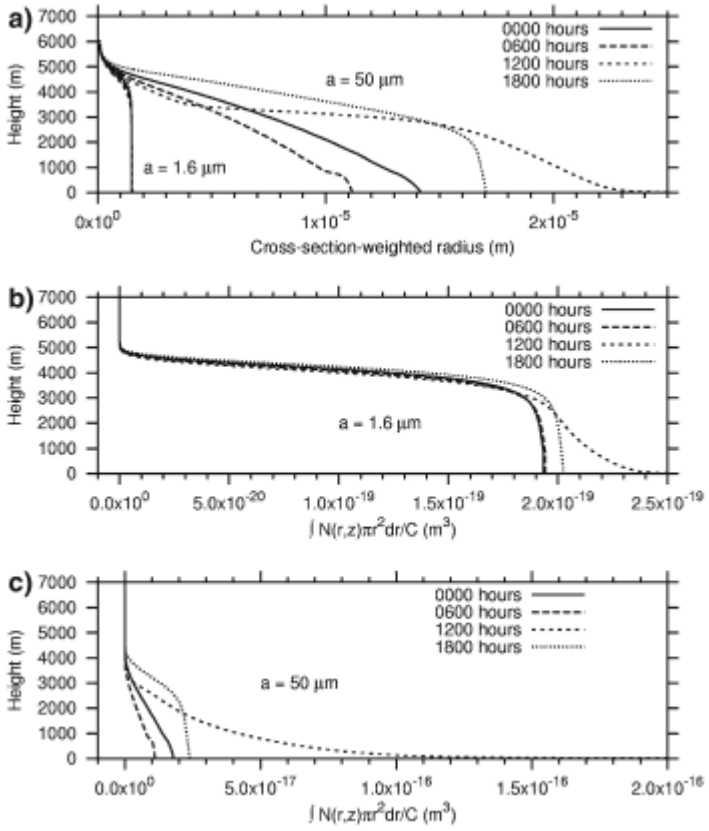

Figure 20: Profiles of, (a) cross-section-weighted mean particle radius, and (b, c) total cross-sectional area per unit volume at indicated times (Mars hours).

Picture taken from[9]

Time	$1.6\mu m$	$50\mu m$
0000	7.83E-16	3.46e-14
0600	7.73E-16	1.94E-14
1200	8.17E-16	11.35E-14
1800	3.28E-16	7.00E-14

Table 5: Values of $\int A(z)dz/C$ from $zlb = 1$ m to infinity (m4) corresponding to the scenarios presented. Note that C has dimensions m−4
Table taken from [9]

$$\tau_\lambda = \int_{zlb}^{\infty} \sigma_\lambda dz \tag{15}$$

For $Q_{r,\lambda} = Q_{ext}(\lambda)$, independent of r, and thus of height, z, we can write

$$\tau_\lambda = Q_{ext} \int_{zlb}^{\infty} A(z)\sigma_\lambda dz \tag{16}$$

where $A(z)$ is the cross-sectional area per unit volume,

$$A(z) = \int_{0}^{\infty} \pi r^2 N(r,z) dr \tag{17}$$

shown (scaled by$C$) in (Figure 20 b, c). Performing the integration's indicated by Equation 16 gives the values for $\tau_\lambda C/Q_{ext}$ given in Table 5. Taking representative values of $Qext$ for the wavelengths and particle sizes considered then allows the determination of the scaling factor C needed to produce a desired optical depth. For example with $Q_{ext} = 2.8$ and optical depth $\tau_\lambda = 0.5$ at 0000 on scenario $1.6\mu m$ we would have $C = \tau_\lambda/(7.83 \times 10^{-16} * Q_{ext}) = 2.28{\times}10^{14} m{-}4$. Values of A(z) corresponding to this value of C within the well-mixed layer are of order $4.4 \times 10^{-5} m - 1$.

The particle size distribution Figure 21 was calculated with the mean mass loading $\eta \approx 1.06^{-5}$ and one meter high from the Mars surface.

Time	$1.6\mu m$	$50\mu m$
0000	2.37E-4	1.51E-4
0600	2.35E-4	1.21E-4
1200	2.47E-4	2.12E-4
1800	2.52E-4	1.94E-4

Table 6: Values of $\int \int Ndzdr/C$ over all r and from $zlb = 1$ m to infinity (m2) corresponding to the scenarios presented
Table taken from [9]

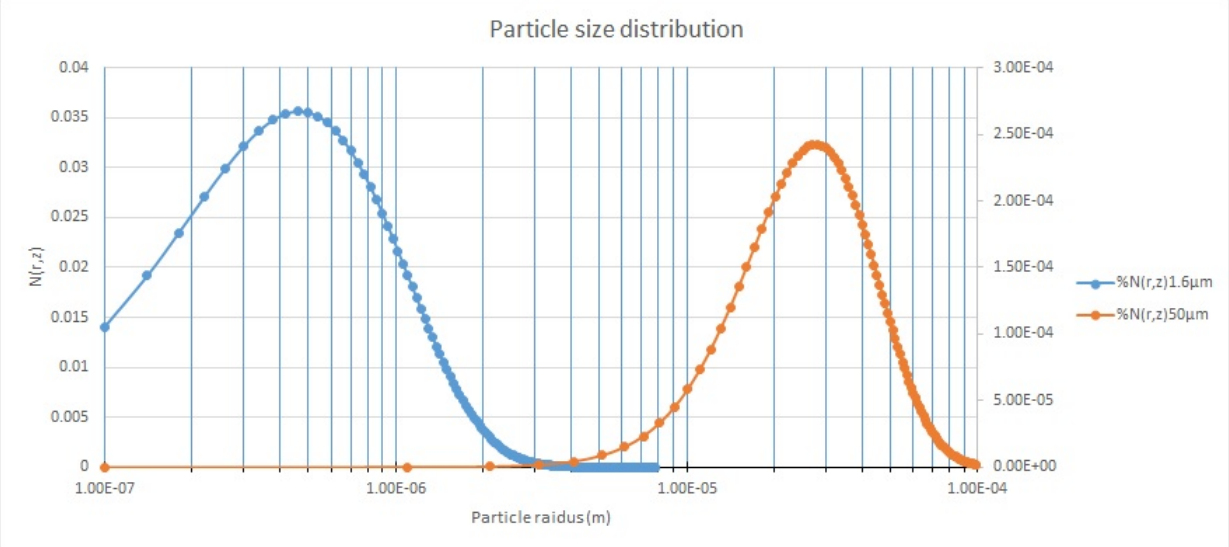

Figure 21: Particle size distribution

2.4 Design of the filter

The filter must be designed for preventing coarser particles in the inlet of the pump blocking the pumping system. In previous works was found that the inlet of the pump should be protected with an HEPA filter (High Efficiency Particulate Air filter) in order to avoid that dust grains block the pump mechanism; anyway no significant problems should occur with particles of size less than 100 μm.[27]

The MicroMed system can measure particles until $30\mu m$ so the filter will be designed for this value as the cutoff diameter.

For calculating the diameter of the impactor sphere for a cut point of $30\mu m$ first we take the stokes number for a round jet impactor Equation 2

$$Stk = \frac{\rho_p C_c d_p^2 U}{9\mu W}$$

Solving the stokes equation for the nozzle diameter W

$$W = \frac{\rho_p C_c d_p^2 U}{9\mu Stk}$$

where
ρ_p =particle density ($2730 Kg/m^3$)
C_c =slip correction(≈ 1)
U =relative velocity of body to gas 7.5m/s
dp =particle diameter($30\mu m$)
μ =gas viscosity (1.5E-5 Kg/(ms))
W =nozzle diameter (circular impactor) or nozzle width (rectangular impactor).

The square root of the Stokes number $\sqrt{Stk}$ corresponding to the 50% collection efficiency $\sqrt{Stk_{50}}$ can be estimated from Figure 13,which shows the theoretical impactor efficiency curves for different values of the jet Reynolds number. We assume a jet Reynolds number of 3000; then the corresponding $\sqrt{Stk_{50}}$ is 0.47 efficiency and W is equal to 617mm.

Knowing the nozzle diameter, the jet Reynolds number is calculated from Equation 5 by substituting the Reynolds jet velocity becomes:

$$Re_j = \frac{\rho_g W U}{\mu}$$

The jet Reynolds number becomes 3240 and is close to the initial assumption of 3000.

This solution is a first approximation to the problem because due to weight and volumetric restrictions the diameter of the sphere can not be 617mm.

2.5 Fluid and Particle dynamics

For calculating the dynamics of the carrier fluid and particles is important to clarify the way in which each of the phases in a two-phases flow is computed. The fluid phase (gas) is modeled as a continuous mean using the Euler approach and the solid phase (particles) is computed using the Lagrangian approach, in the literature this type of procedure is known as Euler-Lagrange approach for two phase flows.

2.5.1 Continuous phase

The gas phase is calculated based on the Euler approach. Mean quantities of the gas phase are found by solving the Reynolds's - average governing equations for conservation of mass and momentum.

$$\nabla \cdot (\bar{\rho}_c \tilde{U}_c) = 0 \tag{18}$$

$$\nabla \cdot (\bar{\rho}_c \tilde{U}_c \tilde{U}_c) = \nabla \cdot (\bar{\rho}_c \mu_{tot} \nabla \tilde{U}_c) - \nabla \bar{P} + \bar{\rho}_c g \tag{19}$$

Where

$\tilde{U}_c$ is the average velocity of the continuous phase

$\bar{\rho}_c$ is the mean density of the continuous phase

μ_{tot} is the sum of the cinematic viscosity μ_c and the turbulent viscosity μ_T

g is the gravitational acceleration

$\bar{P}$ is the mean pressure

Two additional transport equations are solved, one for turbulent kinetic energy k and the other for its dissipation rate ϵ. In fact, in Equation 19 the turbulent viscosity is derived from a turbulence model and it is expressed as:

$$\mu_T = \rho C_\mu \frac{k^2}{\epsilon} \tag{20}$$

$$\frac{\partial}{\partial t}(\rho_c k)+\frac{\partial}{\partial x_j}(\rho_c \epsilon k u_j)=\frac{\partial}{\partial x_j}[(\mu+\frac{\mu_T}{\sigma_k})\frac{\partial}{\partial x_j}]+G_k+G_b-\rho_c\epsilon-Y_M+S_k \quad (21)$$

$$\frac{\partial}{\partial t}(\rho_c \epsilon)+\frac{\partial}{\partial x_j}(\rho_c \epsilon u_j)=\frac{\partial}{\partial x_j}[(\mu+\frac{\mu_T}{\sigma_k})\frac{\partial}{\partial x_j}]+\rho_c C_1 S\epsilon-\rho_c C_2\frac{\epsilon^2}{k+\sqrt{v\epsilon}}+C_{1\epsilon}\frac{\epsilon}{k}C_3 G_b+S_\epsilon \quad (22)$$

$$C_1=max[0.43,\frac{\eta}{\eta+5}\ \ \eta=S\frac{k}{\epsilon}\ S=\sqrt{2S_{ij}S_{ij}}$$

In these equations, G_k represents the generation of turbulence kinetic energy due to the mean velocity gradients. G_b is the generation of turbulence kinetic energy due to buoyancy. Y_M represents the contribution of the fluctuating dilatation in compressible turbulence to the overall dissipation rate. C_2 and $C_{1\epsilon}$ are constants. σ_k and σ_ϵ are the turbulent Prandtl numbers for k and ϵ, respectively. S_k and S_ϵ are user-defined source terms.

$$C_\mu=\frac{1}{A_0+A_s\frac{kU^*}{\epsilon}} \quad (23)$$

$$U*=\sqrt{S_{ij}S_{ij}+\tilde{\Omega_{ij}}\tilde{\Omega_{ij}}} \quad (24)$$

$$\tilde{\Omega_{ij}}=\Omega_{ij}-2\epsilon_{ijk}\omega_k \quad (25)$$

$$\Omega_{ij=}\bar{\Omega_{ij}}-\epsilon_{ijk}\omega_k$$

where $\overline{\Omega_{ij}}$ is the mean rate-of-rotation tensor viewed in a rotating reference frame with the angular velocity ω_k. [1]

Most of the fluid dynamics software solves the Reynolds average Navier -Stokes (RANS) equations.[10][2, 24]

2.5.2 Particle Phase

The motion of the particles is computed using the Lagrangian approach, for the formulation of the particle equation of motion it was assumed the one-way coupling regime, the point particles approximation (the volume occupied by a particle is negligible), and that the forces acting on particles due to particle

Coefficients	Value
A_0	4.04
A_S	$\sqrt{6}\,cos\phi$
$C_{1\epsilon}$	1.44
C_2	1.92
σ_k	1.0
σ_ϵ	1.2

Table 7: Turbulence model constants
Table taken from[2]

rotation, the pressure gradient in the flow, the added mass force and the Basset history force are negligible since a large density ratio $\rho_p/\rho_f \gg 1$ is considered.

Each one of the particles is tracked within the calculated flow field in the previous section, solving the equations for particle position x_p, particle velocity u_p and particle angular velocity ω_p.

$$\frac{dx_p}{dt} = u_p \tag{26}$$

$$m_p \frac{du_p}{dt} = F_p \tag{27}$$

where m_p is the particle mass and F_p the net force . The net force is the sum of different sources that act on the particle which are the drag force and the gravitational force.

The drag force C_D can be calculated as a function of the Re_p using empirical correlations for rigid spheres.

$$C_D = \begin{array}{ll} \frac{24}{Re_p}(1 + 0.15Re_p^{0.687}) & Re_p \leq 1000 \\ 0.44 & Re_p > 1000 \end{array} \tag{28}$$

and the Reynolds number of the particle is defined as:

$$Re_p = \frac{d_P \mid u_c - u_p \mid \rho_p}{\mu} \tag{29}$$

in this approach the instantaneous fluid velocity of the continuous phase u_c is calculated as

$$u_c = U_c + u'$$

the velocity U_c is the one calculate in the previous section and the velocity u_i is the fluctuating velocity of the gas its assumed to have a Gaussian probability distribution with standard deviation related to the turbulent kinetic energy.

On the other hand the gravitational force g is due to the gravitational acceleration and all the particles are subject to this type of force.

$$F_g = m_p g$$

As already notice, other forces due to particle rotation, the pressure gradient in the flow, the "added mass" force and the Basset history force are negligible since a large density difference between the particle and the fluid. The final dynamic equation of the particle motion is

$$m_p \frac{du_p}{dt} = \frac{1}{2} C_D m_p \mid u_c - u_p \mid (u_c - u_p) + m_p g \tag{30}$$

Other important aspect is the time step, as the particle travels a turbulent eddy, the interaction time of this random sampled gas fluctuation velocity component with the particle is limited by the life time of the turbulent eddy T_e, transient time T_r for the particle to traverse the eddy or the particle relaxation time τ_p, all this times scales has to be satisfied in the Lagrangian time step and τ_0 that is the minimum possible value for the time step.

$$\triangle t_L = max(\tau_0, min(T_e, T_r, \tau_p) \tag{31}$$

2.6 Computational domain

For this type of simulations the selected computational domain was as a straigth pipe about one diameter long with the designed filter place in the center. The computational domain is compose of a half circumference of radius 350mm and length 800mm, this was because we want the particles to travel from the injection face into the filter, to accomplish this they have to travel a distance of 400mm. this domain does not allow to reach fully developed flow, but this has not been judged as a strict requirement for this preliminary investigation. Moreover, such a relatively short domain allows performing the simulation whith acceptable computational burden.

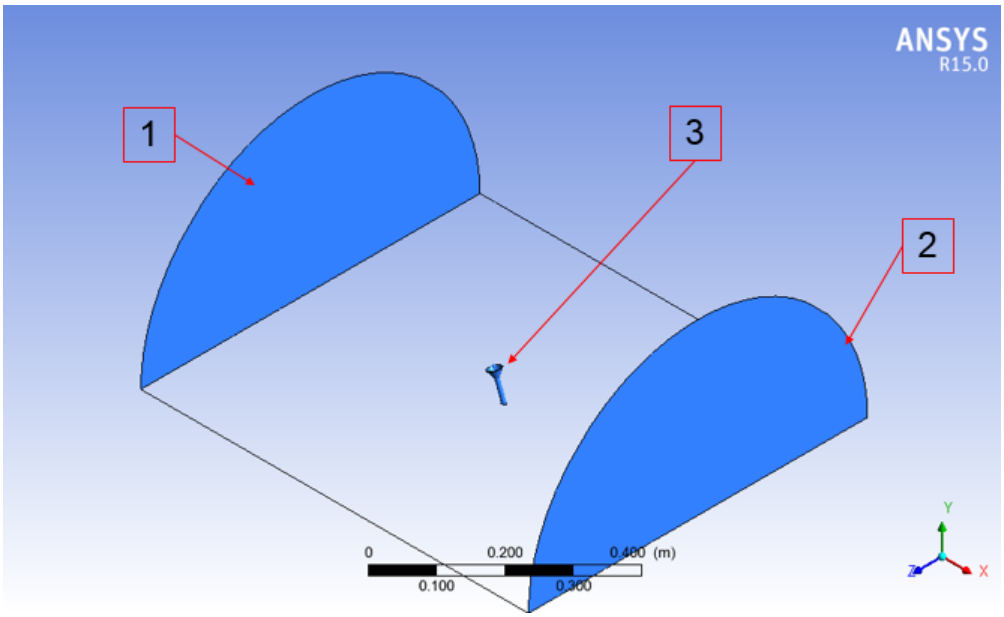

Figure 22: Computational domain

On Figure 22 number one is the inlet of fluid and particles, this face is a semicircle of radius 350mm, number two is the fluid outlet and the distance from face one to face 2 is 800mm and number 3 is the filter.

On Figure 23 face number 4 is used to calculate the efficiency of the filter, face number five is used to measure the mean velocity at the inlet of the filter, face number 6 is used to calculate the number of particles that are collected by the filter and on this face the average velocity generated by the pump is located, and number 7 is the middle point of the pipe and is used for calculate the maximun velocity in the pipe.

2.7 Rosin-Rammler distribution

This type of distribution is used as an input parameter in the defined injections, the required distribution has to be converted to a Rosin-Rammler distribution.

The folowing steps are used to transform a distribution to a Rosin-Rammler type.

- The Rosin-Rammler size distribution is modeled by the mass fraction

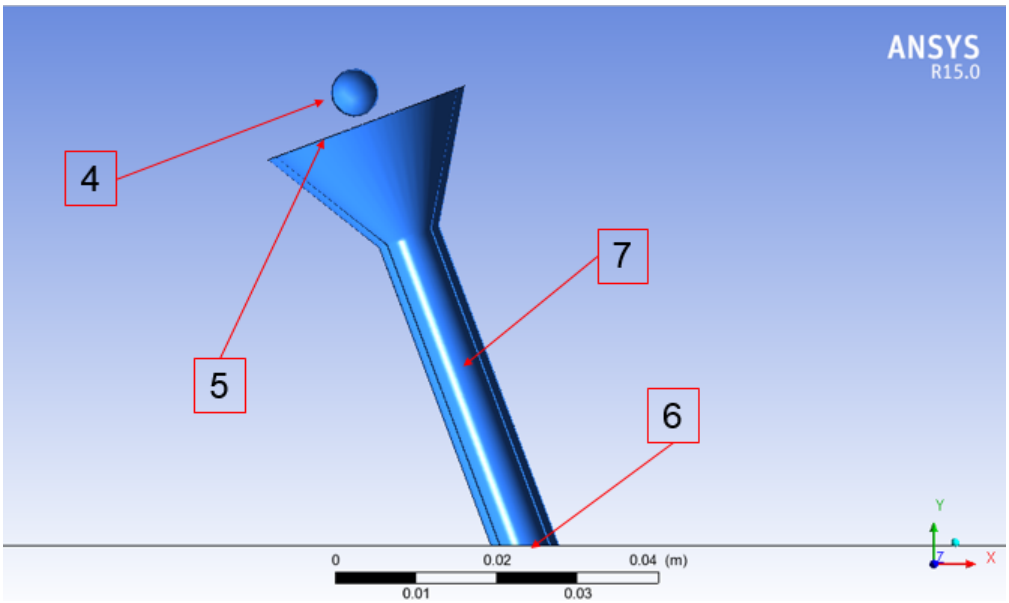

Figure 23: Filter

of droplets of diameter greater than d and its equation is

$$Y_d = e^{-(d/\bar{d})^n} \tag{32}$$

where $\bar{d}$ is the size constant and is the size distribution parameter.

- By default, you will define the size distribution of particles by inputting a diameter for the first and last points and using the linear equation Equation 32 to vary the diameter of each particle stream in the group.

- Your particle size distribution may be defined most easily by fitting the size distribution data to the Rosin-Rammler equation. In this approach, the complete range of particle sizes is divided into a set of discrete size ranges, each to be defined by a single stream that is part of the group.

- The Rosin-Rammler distribution function is based on the assumption that an exponential relationship exists between the droplet diameter, d, and the mass fraction of droplets with diameter greater than d, Y_d.

- To derive values of $\bar{d}$ and n you need a plot of the data of Y_d vs d . The value for $\bar{d}$ is the valued of d at which $Y_d = e^{-1} \approx 0.368$. The numerical value for n is given by

$$n = \frac{ln(-lnY_d)}{ln(d/\bar{d})} \tag{33}$$

- By substituting the given data pairs for Y_d and $d/\bar{d}$ into this equation, you can obtain values for n and find an average.[1]

The CFD software used for this simulation requires that you convert you cumulative size distribution by mass to a Rosin-Rammler distribution for the Discrete phase model (DPM), in this way the particle size distribution of the Mars atmosphere can be converted and introduced into the simulation environment.

2.8 DPM, Boundary and conditions Solution setup

The available boundary conditions, for the discrete phase model (DPM):

- REFLECT

The particle rebounds off the boundary in question with a change in its momentum as defined by the coefficient of restitutionFigure 24.

The normal coefficient of restitution defines the amount of momentum in the direction normal to the wall that is retained by the particle after the collision with the boundary, v_n is the particle velocity normal to the wall and the subscripts 1 and 2 refer to before and after collision, respectively. Similarly, the tangential coefficient of restitution, e_t, defines the amount of momentum in the direction tangential to the wall that is retained by the particle.

A normal or tangential coefficient of restitution equal to 1.0 implies that the particle retains all of its normal or tangential momentum after the rebound (an elastic collision). A normal or tangential coefficient of restitution equal to 0.0 implies that the particle retains none of its normal or tangential momentum after the rebound[1].

- TRAP

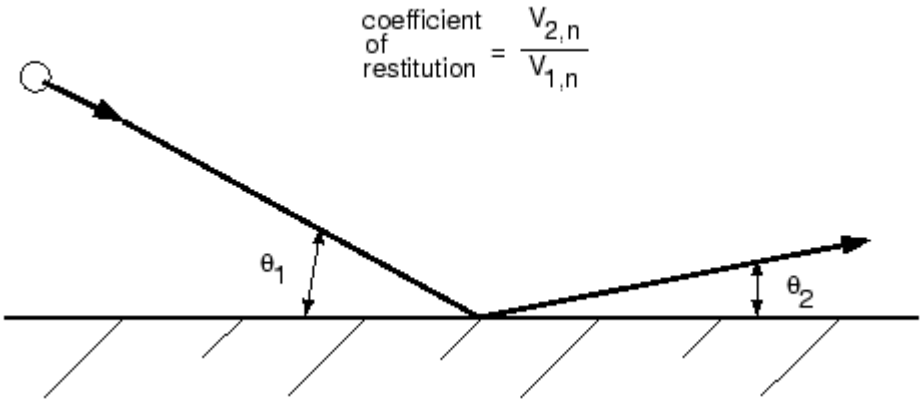

Figure 24: Reflect Boundary Condition for the Discrete Phase
Picture taken from[1]

The trajectory calculations are terminated and the fate of the particle is recorded as "trapped". In the case of evaporating droplets, their entire mass instantaneously passes into the vapor phase and enters the cell adjacent to the boundary. See Figure 25 In the case of combusting particles, the remaining volatile mass is passed into the vapor phase.

- ESCAPE

The particle is reported as having "escaped" when it encounters the boundary in question. Trajectory calculations are terminated. See Figure 26.

For the solution setup was used the values provided by the literature in this type of simulations,

- solver: Pressure Based

  Velocity formulation: Absolute

  Time: Steady

- The models where

  Viscous model

  K epsilon (2eqn)

  Realizable with standard wall functions

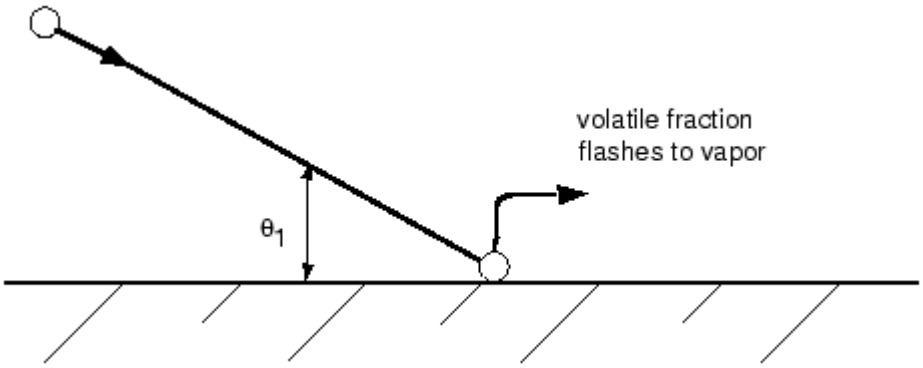

Figure 25: "Trap" Boundary Condition for the Discrete Phase
Picture taken from [1]

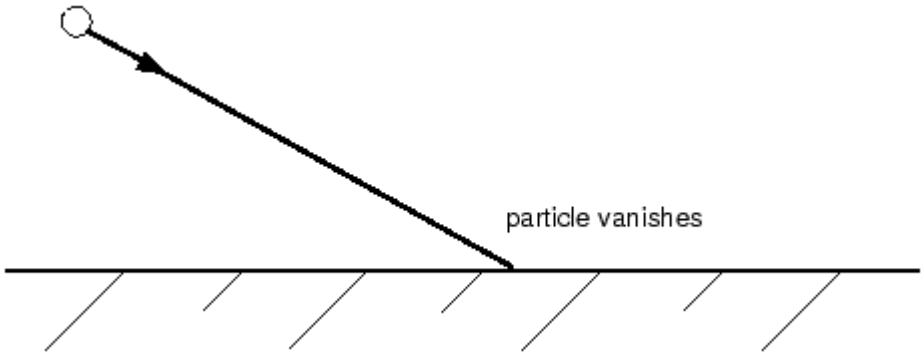

Figure 26: "Escape" Boundary Condition for the Discrete Phase
Picture taken from [1]

Injection	0	1
Release from	Face 1 in	Face 1 inp
Velocity magnitude	7.5 m/s	7.5 m/s
Total flow rate	4.19E-9 kg/s	1.66E-6 kg/s
Min diameter	1E-07 m	1E-6 m
Max diameter:	1E-05 m	1E-4 m
Mean Diameter:	4.24E-06	8.5E-5 m
Spread factor	2.3	5.3

Table 8: Injections Values
The values calculated for the injections are the ones explained with the Rosin-Rammler distribution

- Discrete phase

  Maximum number of steps:1e+06

  Length scale:1e-07

  discrete random walk model is activated with 30 tries, and 0.15 time scale constant.

The values used for the injections are the ones inTable 8, these two particle groups are defined to simulate the Martian atmosphere, the injections one with $b = 0.2$, as mean radius $a = 1.6\mu m$ that represents the particles that slowly settles out while being mixed through the boundary layer by turbulence as a first source of the aerosol, for the second one a much coarser dust with $a = 50\mu m$ and $b = 0.2$ represents the dust created in the surface, then converting this distribution to a Rosin-Rammler distribution to introduce in the software. These two injections represents the martian particle distribution at $1m$ above the surface and both of them are released from face 1 at the same time.

The boundary conditions used for this simulations are describe in Table 9.

- Solution methods

  Scheme: Coupled

  Gradient: Green-Gauss Node Base

  Pressure:PRESTO

  Momentum: Second order Upwind

Face	Name	Type	Value	DPM
1	inp	Velocity inlet	7.5 m/s ,magnitude normal to Boundary	escape
2	outf	Pressure-outlet	5% Back flow intensity, 10 back flow turbulent viscosity ratio	escape
6	out	Velocity inlet	4 m/s, direction X:0.364; Y:-1	trap
3	pipe	wall	wall	reflect
	outherwall	wall	wall	escape

Table 9: Boundary conditions

Turbulent kinetic energy: First order Upwind

Turbulence dissipation rate: First order Upwind

All the residual where set to 1e-6.

2.9 Efficiency

- The aspiration efficiency, of a given particle size is defined as the concentration of the particles of that size in the gas entering the inlet divided by their concentration in the ambient environment from which the sample is taken.

- The transmission efficiency, of a given particle size is defined as the fraction of aspirated particles of that size that are transmitted through the inlet to the rest of the sampling system.

- The inlet efficiency, is the product of the inlet and transmission efficiencies and is the fraction of the ambient concentration that is delivered to the aerosol transport section of the sampling system by the inlet.

$$\eta_{inlet} = \eta_{asp}\eta_{trans} \tag{34}$$

The adopted procedure (Figure 27) is as follows: first we have to calculate the particle size distribution of the aerosol, the software calculates a

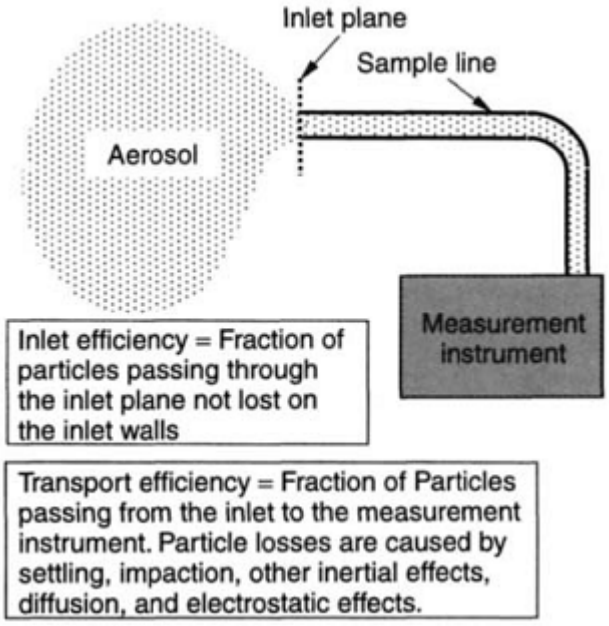

Figure 27: Representative sampling of aerosol to make accurate measurements

Picture taken from[21]

histogram by number of particles and it radius (Figure 28), we want this histogram in face 1 that is the inlet of particles to the system, then converting this distribution to a volume distribution with Equation 10, we do the same procedure to the particles on face 6 , this particles are the ones collected by the filter and finally we calculate this procedure for face 4.

The aspiration efficiency is defined as the concentration of particles of a given size entering the inlet divided by the concentration in the ambient environment, the amount of particles in the inlet are the ones that actually get inside (face 6) and the ones that impact in the sphere (face 4), this two divided by the ones on the aerosol (face 1).

for the transmission efficiency you have the fraction of particles transmitted into the system (face 6) and those that could be transmitted (face4 + face 6).

Finally we use Equation 34 to calculate the inlet efficiency, in this procedure you calculate the efficiency only in one for one diameter interval of particles, but not always the intervals are the same between the particle size distribution for this reason to have the information in the same intervals you have to use a linear interpolation of the data, in this way you have all the data in the same intervals and the efficiency can be calculated. [3, 21]

2.10 Grid convergence index (GCI)

The appropriate level of grid resolution is a significant issue in numerical investigations. It is a function of many variables including the flow condition, type of analysis, geometry and many other variables. The GCI is based upon a grid refinement error estimator derived from the theory of the generalized Richardson extrapolation . The GCI is a measure of how far the computed value is away from the value of the asymptotic numerical value. Consequently, it indicates how much the solution would change with a further refinement of the grid. A small value of GCI indicates that the computation is sufficiently close to the exact (asymptotic) solution.[4]

The GCI method requires that the numerical solution satisfies the following conditions:

- The flow field is sufficiently smooth to justify the use of Taylor series expansions (i.e. no discontinuities in any of the flow variables).
- The convergence is monotonic (i.e. if the value of a target quantity increases/reduces by an amount X upon going from a coarse mesh to a

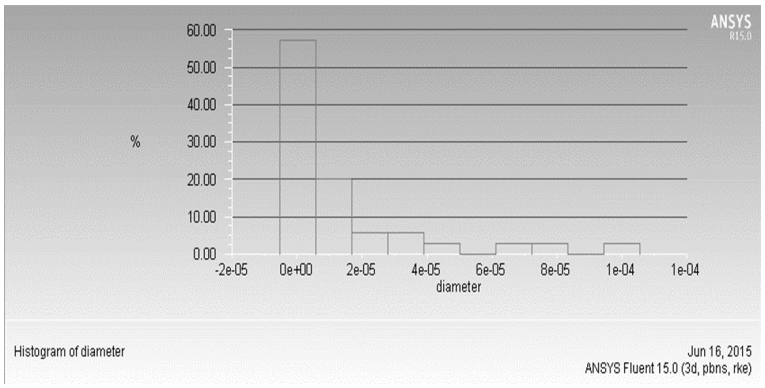

(a)

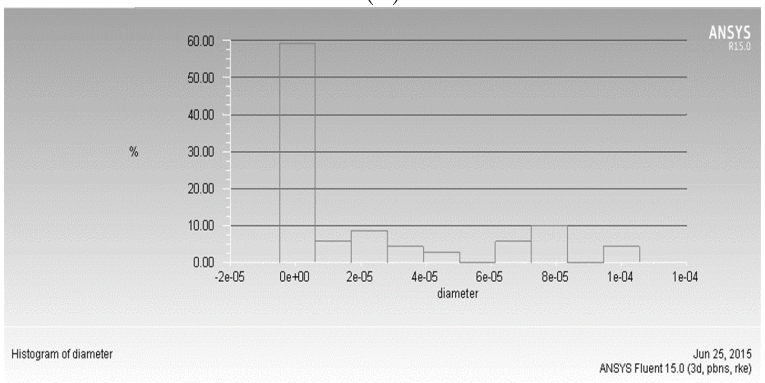

(b)

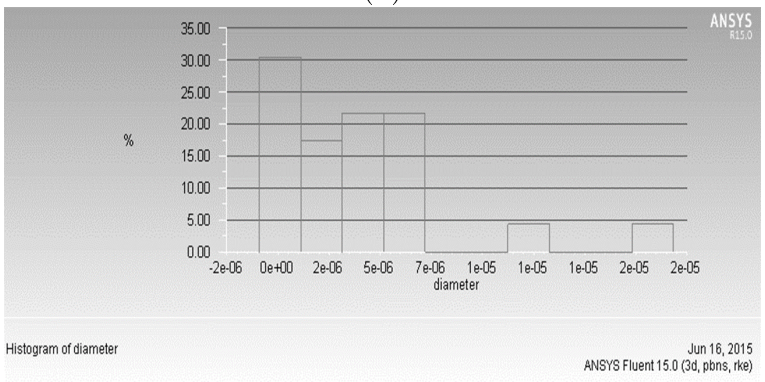

(c)

Figure 28: Histogram
(a) Face1: total number = 35639, mean = 1.42977e-05, min = 1e-07 , max = 0.0001, sum = 0.509555, standard deviation = 2.35617e-05
(b) Face4: total number = 35639 mean, = 1.42977e-05, min = 1e-07, max = 0.0001, sum = 0.509555, standard deviation = 2.35617e-05
(c) Face6: total number = 35639, mean = 1.42977e-05, min = 1e-07, max = 0.0001, sum = 0.509555, standard deviation = 2.35617e-05

medium mesh, its value should again increase/reduce upon going from the medium mesh to a fine mesh and the magnitude of the change should be smaller than the magnitude of X).

- The numerical method is in its asymptotic range (i.e. the leading term of the Taylor series expansion dominates the truncation error behavior).[25]

The GCI on the fine grid is defined as:

$$GCI_{i,i+1}^{fine} = \frac{F_s \mid \varepsilon_{i,i+1} \mid}{r_{i,i+1}^{p} - 1} \tag{35}$$

where F_s is a factor of safety. $F_s = 3$ for comparison of two grids and 1.25 for comparison over three grids or more, ε is a relative error measure of the key variable f between the coarse and fine solutions

$$\varepsilon_{12} = \frac{f_2 - f_1}{f_1} \tag{36}$$

where f_2 is the coarse-grid numerical solution obtained with grid spacing h_2. f_1 is the fine-grid numerical solution obtained with grid spacing h_1. r is the grid refinement ratio ($r_{12} = h_2/h_1 > 1$). For 3-Dimensional geometries $r_{12} = (\frac{N1}{N2})^{1/3}$,$r_{23} = (\frac{N2}{N3})^{1/3}$, $e_{12} = f_2 - f_1$,$e_{23} = f_3 - f_2$

The apparent order of convergence p is calculated using the iterative technique with relaxation factor w.

$$p = w\rho + (1 - w)\frac{ln(\beta)}{ln(r_{12})} \tag{37}$$

where $\beta = \frac{(r_{12}^{p}-1)e_{23}}{(r_{23}^{p}-1)e_{12}}$, $w = 0.5$ and ρas the previous iteration of p. The first iteration of ρ can be $\rho = ln(\frac{e_{23}}{e_{12}})/ln(r_{12})$.

Now we can caclculate$\varepsilon_{12} = \frac{f_2-f_1}{f_1}$,$\varepsilon_{23} = \frac{f_3-f_2}{f_2}$, and $GCI_{23}^{fine} = \frac{1.25|\varepsilon_{23}|}{r_{23}^{p}-1}.GCI_{12}^{fine}$ should be smaller thanGCI_{23}^{fine}, to check if the solution is in the asymptotic range $\alpha \approx 1$ Equation 38.

$$\alpha = r_{12}^{p}\frac{GCI_{12}^{fine}}{GCI_{23}^{fine}} \tag{38}$$

and the ratio R Equation 39 must be less than unity.

		N_i	f_i	$r_{i,i+1}$	$e_{i,i+1}$	$\varepsilon_{i,i+1}$	$GCI_{i,i+1}^{fine}$	R	α
Max velocity pipe	0		7.82					3.50E-01	9.72E-01
	1	1314897	7.78	1.268	7.53E-02	0.98%	0.69%		
	2	645756	7.70	1.275	2.17E-01	2.90%	1.96%		
	3	311234	7.49						
Effitiency	0		40.51					8.77E-02	8.69E-01
	1	1314897	40.44	1.268	5.60E-01	1.40%	0.20%		
	2	645756	39.88	1.261	5.22E+00	15.06%	2.25%		
	3	311234	34.66						
$\sqrt{Stks_{50}}$	0		3.54					9.14E-02	6.55E-01
	1	1314897	3.51	1.268	1.70E-01	5.09%	1.03%		
	2	645756	3.34	1.261	1.15E+00	52.77%	11.30%		
	3	311234	2.19						

Table 10: Grid convergency calculations using GCI method and three grid levels

$$R = \varepsilon_{12}/\varepsilon_{23} \tag{39}$$

The Richardson extrapolation can be used to obtain the value of f at grid spacing tend to 0 (Number of elements $N \to \infty$).

$$f_0 = f_1 + \frac{(f_1 - f_2)}{(r_{12}^p - 1)} \tag{40}$$

Table 10 presents the grid convergency calculations using GCI method and three grid levels . In Figure 29 (a) the maximum velocity in the pipe is locate in face 7, for Figure 29 (b) show the inlet efficiency of the filter and $\sqrt{Stk}$ number, this variables was selected to obtain an independent grid solution. The following conclusions have been obtained from the GCI analysis:

- The results are in the asymptotic range , because the obtained values for α are close to unity.
- The ratio R is less than unity this means monotonic convergence.
- There is a reduction in the GCI value for the successive grid refinements (GCIfine 12 $<$ GCIfine 23) for the two variables. This indicates that the dependency of the numerical results on the cell size has been

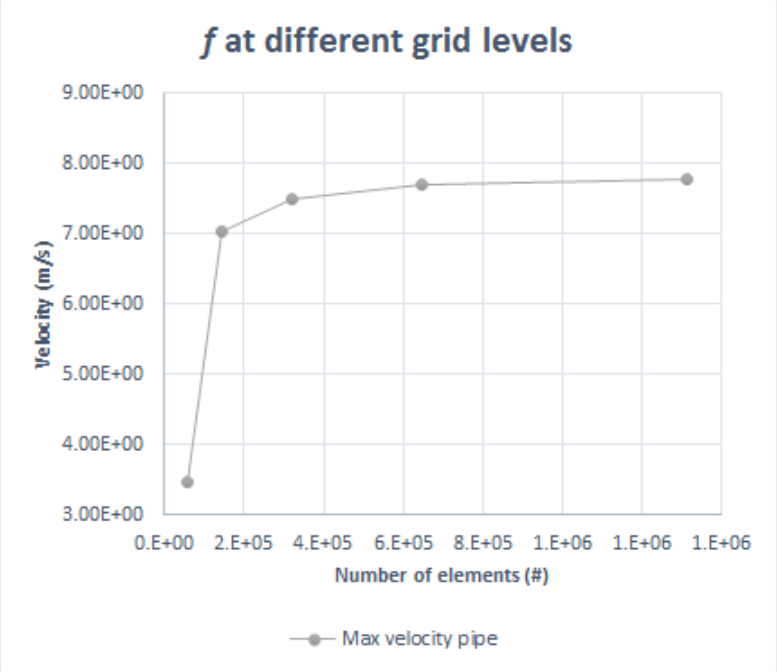

(a)

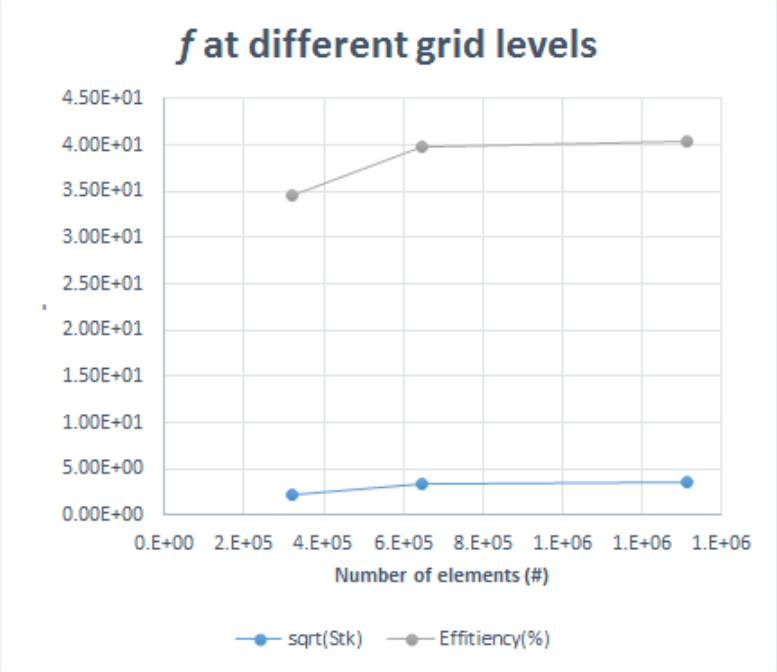

(b)

Figure 29: f at different grid levels:
(a) Max velocity in the pipe
(b) $\sqrt{Stk}$and Overall efficiency

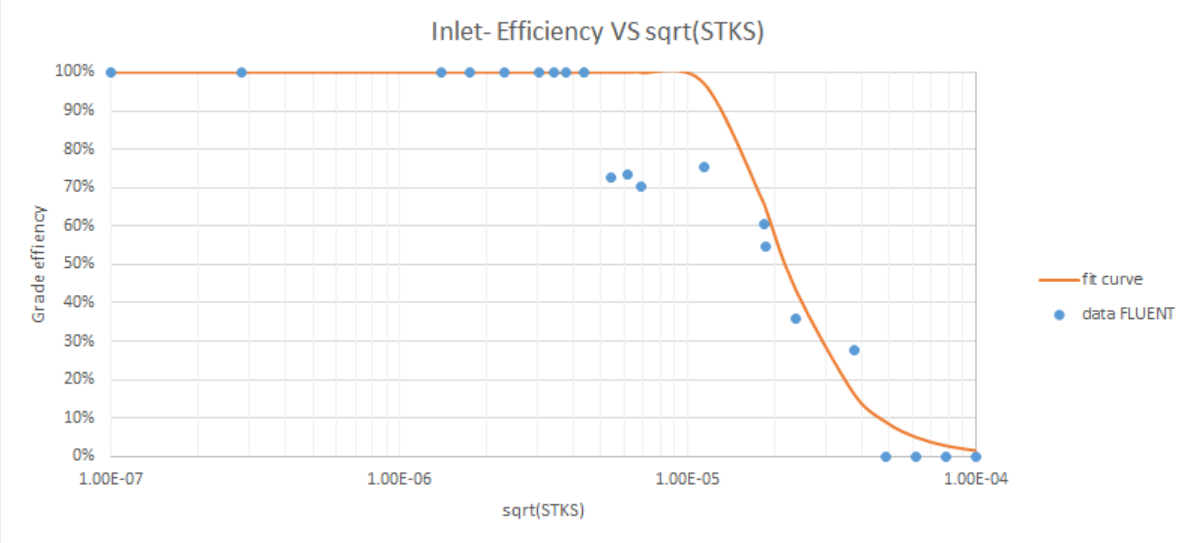

Figure 30: η_{inlet}VS $\sqrt{Stk}$

reduced. The low values of the GCI indexes indicates that the finest mesh is capable of providing a grid independent solution, at least with respect to the investigated variables. Further refinement of the grid will not give much change in the simulation results. For the extrapolated values f_0 is only slightly different from the finest grid solution, as it is lower only with respect to the "mean velocity inlet". Therefore, the solution has converged with the refinement from the coarser grid to the finer grid.

2.11 Results

For this results all residuals where set to 1e-6, the simulations where performed in a i7-3630QM of 2.4 GHz and a simulation time of 3 hours for the fluid phase and 4 hours to the DMP, in a mesh of 1.2e-6 elements and all the simulations where made whit more than 7e5 elements.

The solutions obtained shows the behavior of the fluid, in Figure 31 (c) the velocity magnitude of the fluid, in Figure 31 (a) the Path lines and Figure 31 (b) the vectors of the fluid domain that describes the motion of the fluid around the filter.

The results are measured with the inlet efficiency, this efficiency change

Efficiency	33.05%	40.44%	51.65%	48.16%
#Diameters	10	20	30	40
Total particles	25443	35639	52986	74520
Number particles Face 4	18	23	30	44
Number of particles Face 6	72	71	66	107

Table 11: Values for different number of diameters

with respect to the number of particles in Face 1, 4 and 6 for this reason a statistics analysis was performed changing the number of particles in the domain, to accomplish this, the number of diameters in the Rosim-Rammler distribution was changed (Table 11). The number of diameter is defined as "Each atomizer in the injections, use a Rosin-Rammler distribution for the particles exiting the injector. In order to decrease the number of particles necessary to accurately describe the distribution, the diameter distribution function is randomly sampled for each instance where new particles are introduced into the domain".

So, increasing the number of particles have a more significant effect on the filter efficiency, the filter efficiency tends to stabilize somewhere around 48-52%.The average of the efficiency is 43.32% and the deviation is 7.18%.

In the other hand if you run the same simulation several times the simulation data change in an small quantity for 4 simulations the average efficiency is is 40.36% with deviation 0.12% this is due to the turbulent dispersion that is of minor importance.

Figure 30 show the trend of the inlet efficiency , in this case the inlet efficiency of the filter is $\eta_{inlet} = 40.44\%$ with a cut-off diameter of $d_{50} = 2.2e-5m$.

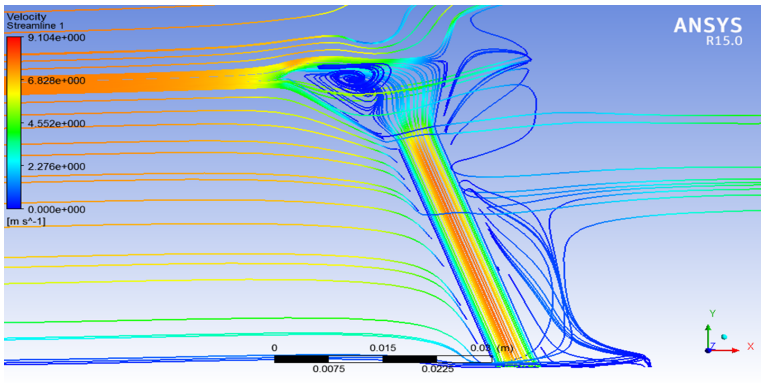

(a)

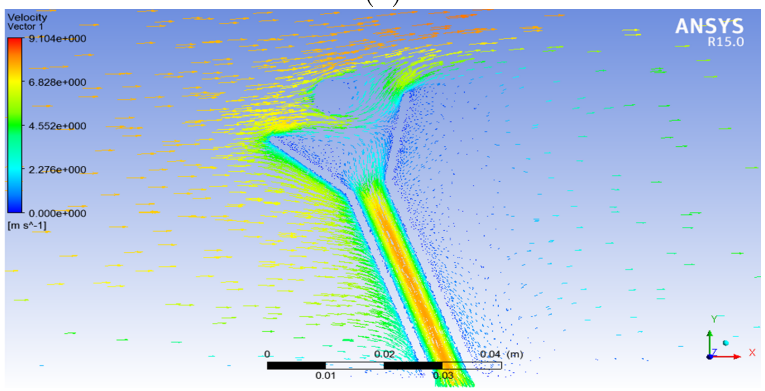

(b)

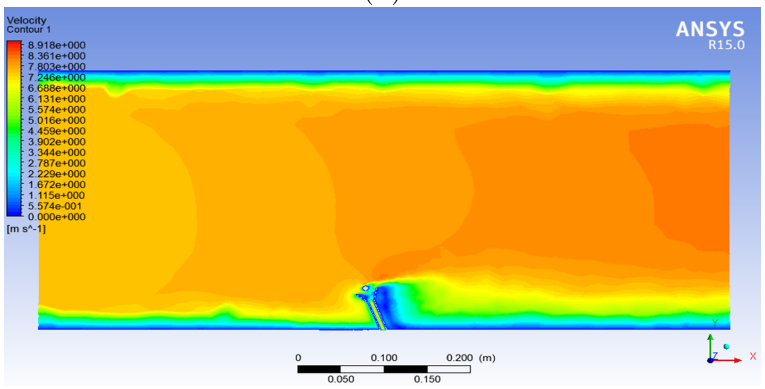

(c)

Figure 31: Velocity field
(a) Path lines by velocity
(b) Velocity vectors
(c)Velocity Magnitude

3 Mechanical design of the inertial filter

The design requirements of the inertial filter (Figure 32) are imposed by the take off from Earth and landing on Mars; the first requirement is to withstand the forces of the take off and landing that are 100 times the Earth gravity, so the quasi static loading analysis is performed to verify that this constraint is fulfilled. The second design criterion is related to the vibrations of the system, the first vibration mode has to be greater than 300Hz to avoid dangerous forcing at low frequency, and the last criteria is the structural resistance of the system, for this analysis the critical buckling load must be greater than 2. All the design conditions has to be accomplished for this work.

For the mechanical design two different solutions are going to be studied in this thesis work, the first one is the filter with 0.25mm wall thickness and the second is 0.5mm wall thickness.

3.1 Quasi-static Analysis

Quasi-static analyses have been performed to compute stresses on the filter under the quasi-static loading of $981 m/s^2$. The finite element models are built with PTC Creo.

The constraint at the mounting interface has been considered infinitely rigid in order to calculate the stresses of the system; this assumption is a worst case condition. The acceleration has been applied along the three directions, X,Y and Z. Maximum value of Von Mises stress is about 16MPa for a wall thickness of 0.25mm and 11.2MPa for a wall thickness of 0.5mm (Figure 33) and it is lower than the admissible limit of the Aluminum 7075-T6 (Table 12). The maximum stress is achieved in the region where the change of section is abrupt, this can be minimized by some rounding in the final design of the filter.In accordance to the ECSS-E-30 Part 3A, the Margin of Safety (MOS) Equation 41 requirement is satisfied with and impose Factor Of Safety(FOS=1.25), resulting in a MOS of about 24 for the first case and 33 for the second case.

$$MOS = \frac{allowable\,stress\,limit}{actual\,stress\,X\,FOS} - 1 > 0 \tag{41}$$

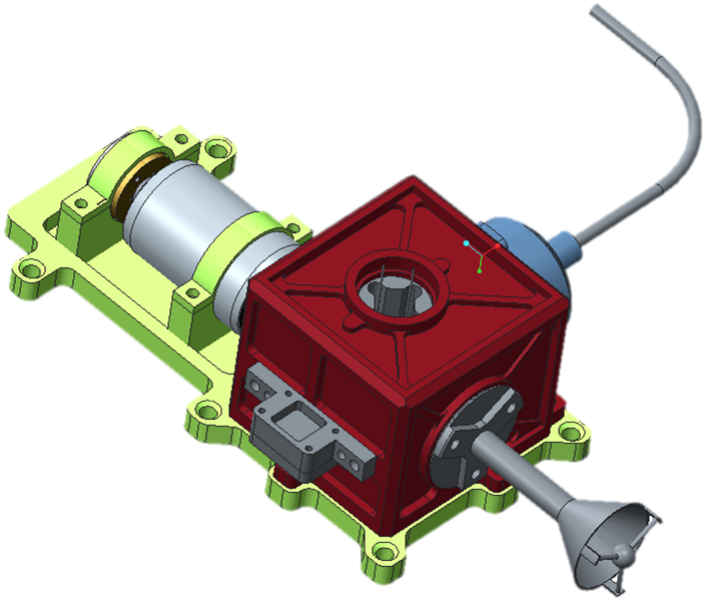

(a)

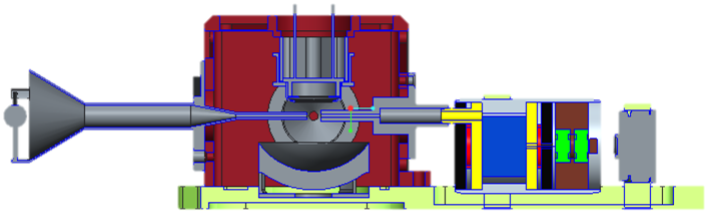

(b)

Figure 32: MicroMed system
(a) 3D Isometric
(b) Mid line plane

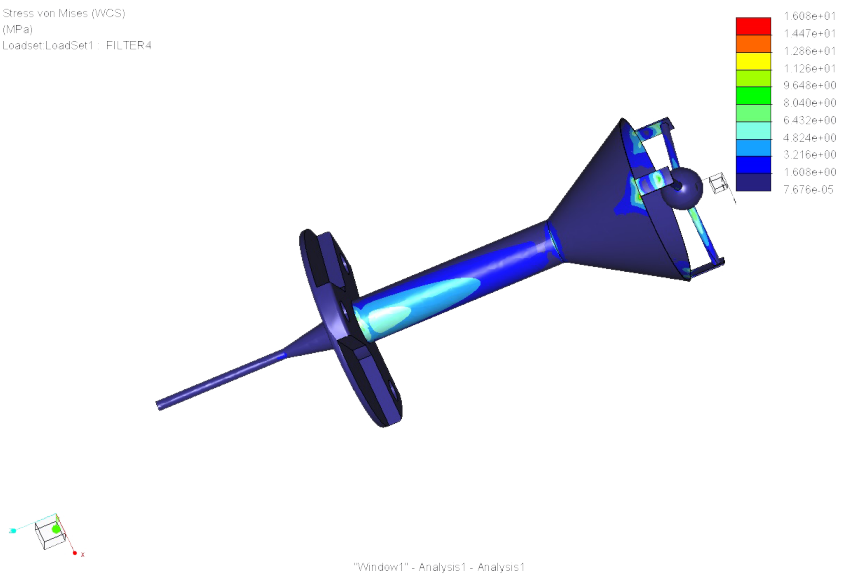

(a)

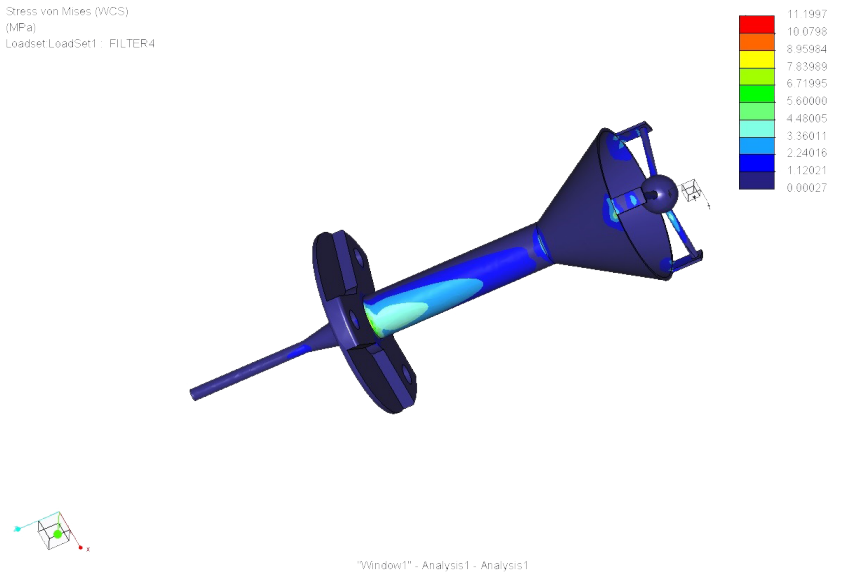

(b)

Figure 33: Von Mises Stress for wall thickness 0.25 (a) and 0.5(b) mm

Frequency range [Hz]	PSD$[g^2/Hz]$
20-100	+3dB/octave
100-300	0.52
300-2000	-2.5 dB/octave

Table 13: Random vibration PSD

Aluminum 7075-T6; 7075-T651		
Density	g/cm3	2.81
Ultimate Tensile Strength	MPa	572.00
Tensile Yiel Strength	MPa	503.00
Modulus of Elasticity	GPa	71.70
Poisson's Ratio		0.33
CTE Linear	µm/m/K	23.60

Table 12: Material Data sheet
Table taken from [23]

3.2 Modal Analysis

In addition to the quasi-static acceleration loads, the component has to withstand random stresses in the range between 20 Hz and 2000 Hz with Power Spectral Density function defined in Table 13.

The lower limit of the first natural frequency of the system equal to 300 Hz; for this reason a frequency analysis must be conducted in order to verify that the first natural frequency of the structure is higher than the critical value of 300 Hz. PTC Creo has been used to perform the frequency analysis. A preliminary modal analysis has been realized considering the bearing like fixed supports (infinitely rigid). In this condition the obtained mode of vibration summarized in Table 14, know for the first natural frequency is equal to 1029 Hz for wall thickens of 0.25 mm and 1321Hz for wall thickness 0.5mm(Figure 34).

The first and second vibration mode for both cases are really close, this vibrations modes are the frequencies in which the main pipe of the filter is moving, mode 1 moves up and down and in mode 2 it moves from side to side, the third vibration mode is related to the movement of the sphere and in both cases the frequency is higher than in the second vibration mode.

The modal analysis performed on the filter shows that the fist vibration

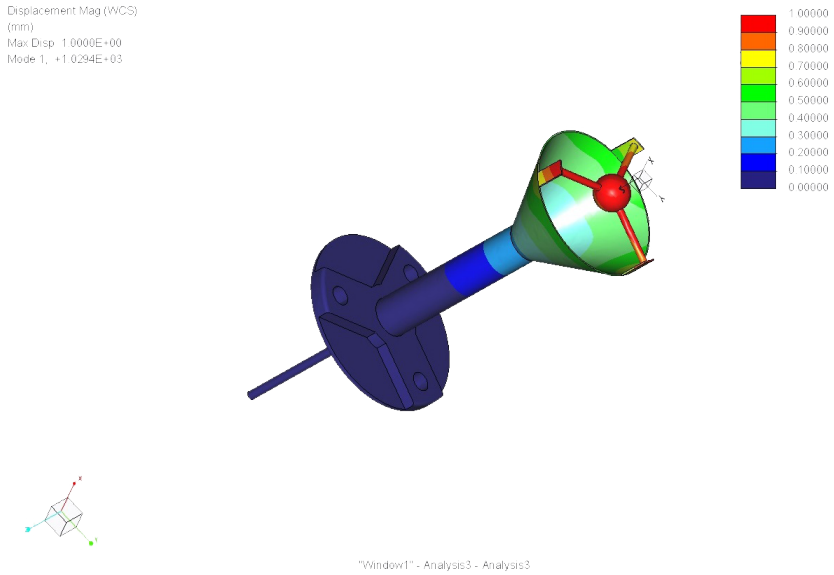

(a)

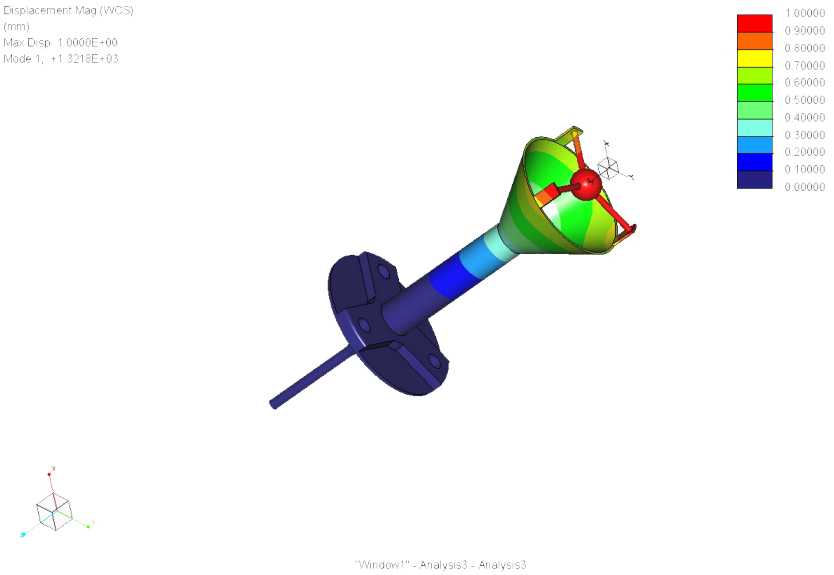

(b)

Figure 34: First vibration mode for wall thickness 0.25 (a) and 0.5(b) mm

	0.5mm Thickness	0.25mm Thickness
Mode 1	1321Hz	1029Hz
Mode 2	1322Hz	1030Hz
Mode 3	2838Hz	2120Hz

Table 14: Vibration mode of the system

mode is grater than 1000Hz in both cases and the condition of the critical value of 300Hz is achieved, and for the design the wall thickness can be reduced until the manufacturing limits allow.

3.3 Buckling analysis

The buckling analysis is carried out to observe the resistance of the filter aginst expected quasi-static loading, in this case the constant has to be greater than 2. For the wall thickness of 0.25mm (Figure 35 a)the coefficient is 483 and for for wall thickness 0.5mm (Figure 35 b) the coefficient is 1806. Thus the buckling condition is not critical for the design study .

3.4 Results

The mechanical design of the filter is limited by manufacturing constraints, under the quasi static analysis the maximum von Mises stress is 16 MPa and the margin of safety is 24, in the frequency analysis the first vibration mode is much higher than 300 Hz, and in the buckling analysis the coefficient is much greater than 2. From this point of view we can reduce the thickness of the walls as much as we want but taking into account the manufacturing constrains of the element, the part that is going to be attached to the optical stage is more bulky because for the manufacture is needed a holding place, also the sphere is attached to the body of the filter by the use of three threaded bars to fix the sphere in the right position. The mass of the filter with wall of 0.25mm is 4.8g and in the case of 0.5 mm is 5.92g, and so not critical for the instrument mass budget (500g with electronics).

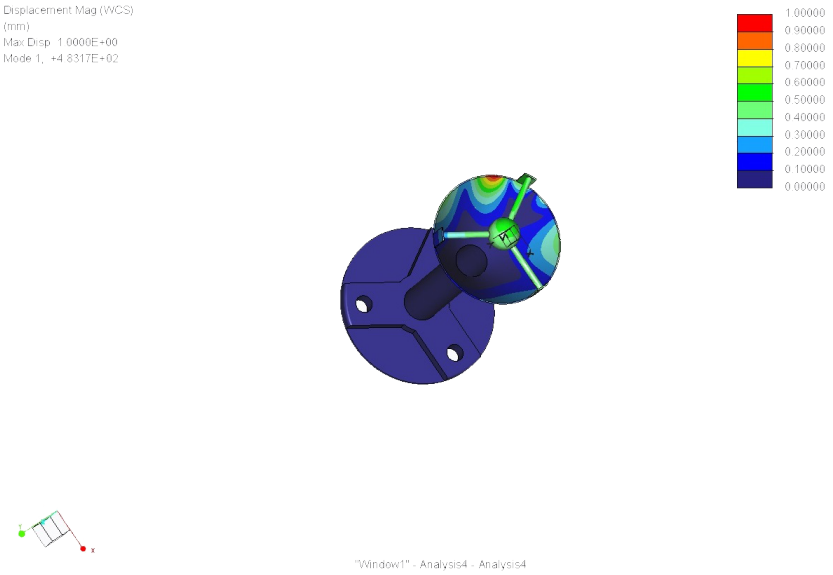

(a)

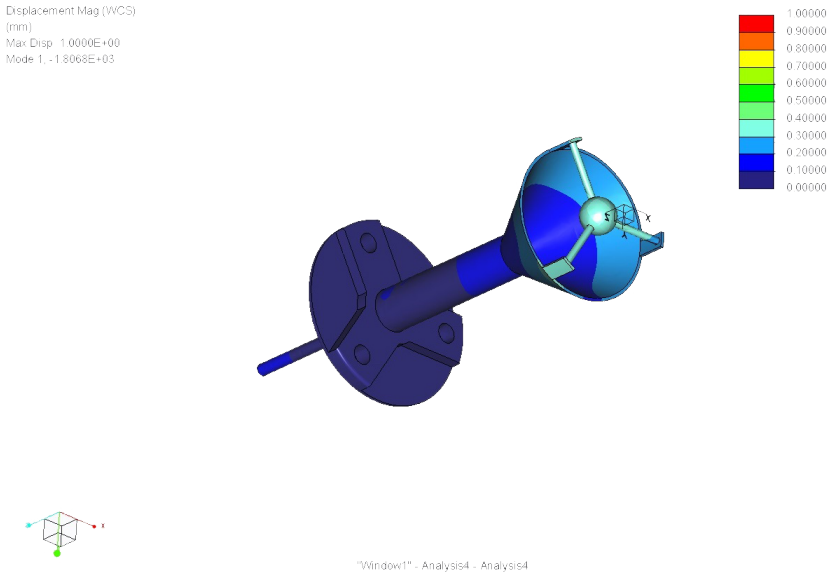

(b)

Figure 35: buckling coefficient 0.25 (a) and 0.5(b) mm

4 Conclusions

This work allowed the design of an inertial filter for a space instrument devoted to dust analysis in Martian environment. The results of the fluid dynamic design show that the efficiency of the filter stabilizes somewhere in between 48-52% with a cut off diameter of 2.2e-5m, so that the coarse particles are not getting into the optical stage, allowing correct working of the instrument. Moreover, the pumping system can be protected as well and additional analyses are required to reduce pressure losses of the pipeline. Moreover is important to notice that all the design was done in average condition of the Martian atmosphere and the efficiency also must be measured in the extreme conditions of Mars. Thus, some experimental activity is needed to verify the obtained results.

The results from the mechanical design show that the filter is able to withstand the forces generated in the take off from Earth and landing to Mars. Additional analyses have to be performed to verify resistance and mechanical stiffness with the overall instrument, i.e. with the filter mounted over MicroMed optical head.

References

[1] *FLUENT 6.3 User's Guide.* 2006.

[2] *An Introduction to Computational Fluid Dinamics.* PEARSOSN prentice Hall, 2007.

[3] *Gas cyclones and swirl tubes, priciples design and operation.* springer, 2008.

[4] Khairy Elsayed. *Analysis and Optimization of Cyclone Separators Geometry Using RANS and LES Methodologies.* PhD thesis, VRIJE UNIVERSITEIT BRUSSEL, 2011.

[5] Chicarro A. et al. The role of dust in the martian climate. 2012.

[6] Colangeli L. et al. Medusa: The exomars experiment for in-situ monitoring of dust and water vapour. *Planetary and Space Science*, 57:1043–1049, 2009.

[7] F D'Amato. et al. Micromed: A compact dust detector for martian airborne dust investigation. 2012.

[8] Forget F. et al. Planet mars - story of another world. *Springer,*, 2006.

[9] Peter A. et al. Modelling dust distributions in the atmospheric boundary layer on mars. *Springer,*, 2007.

[10] Messa Gianadrea. *Two-fluid model for solid-liquid flows in pipeline systems.* PhD thesis, Politecnico di Milano, 2013.

[11] NASA gov. Planet seassons. http://www.nasa.gov/audience/ foreducators/postsecondary/features/FPlanetSeasons.html/, 2014.

[12] NASA gov. What is mars. https://www.nasa.gov/audience/forstudents/5-8/features/what-is-mars-58.html/, 2015.

[13] ESA int. Edm science package and science investigations. http://exploration.esa.int/mars/48898-edm-science-payload/, 2014.

[14] ESA int. Exomars mission (2018). http://exploration.esa.int/mars/48088-mission-overview/, 2014.

[15] ESA int. Exomars orbiter and edm mission (2016). http://exploration.esa.int/mars/46124-mission-overview/, 2014.

[16] ESA int. The exomars programme 2016-2018. http://exploration.esa.int/mars/46048-programme-overview/, 2014.

[17] ESA int. Exomars rover. http://exploration.esa.int/mars/45103-rover-instruments/, 2014.

[18] ESA int. The exomars rover instrument suite. http://exploration.esa.int/mars/45084-exomars-rover/, 2014.

[19] ESA int. Facts about mars. http://www.esa.int/our-activities/space-science/mars-express/facts-about-mars, 2014.

[20] ESA int. Schiaparelli: the exomars entry, descent and landing demonstrator module. http://exploration.esa.int/mars/47852-entry-descent-and-landing-demonstrator-module/, 2014.

[21] Baron A Willeke K, editor. *Aerosol Measurement Principles, Techniques, and Applications*, chapter 10 Inertial, Gravitational, Centrifugal and Thermal Collection Thechniques. WileyInterscience, 2001.

[22] LMD/OU/IAA/ESA/CNES. Mars climate datatabase. http://www-mars.lmd.jussieu.fr/mars/access.html, 5.2 Web Interface.

[23] Matweb. Aluminum 7075-t6; 7075-t651. http://asm.matweb.com/search/SpecificMaterial.asp?bassnum=MA7075T6, 2015.

[24] Mohamed Ali Mergheni, H. Ben Ticha, J. C. Sautet, and Sassi Ben Nasrallah. Interaction particle turbulence in dispersed two phase flows using the eulerian lagrangian approach. *International Journal of Fluid Mechanics Research*, 35(3):273 286, 2008.

[25] P. J. Roache. Quantification of uncertainty in computational fluid dynamics. *Annual Review of Fluid Mechanics*, 29:123–160, 1997.

[26] Planetary science. Internal structure of mars. http://planetary-science.org/mars-research/internal-structure-of-mars/, 2015.

[27] Ventura Sergio. *The MEDUSA and MicroMED experiments for the ExoMars space programe to perform in situ analysis of martian dust.* PhD thesis, Universita degli studi di Napoli Federico II, 2011.